SANDIA REPORT

SAND2004-0074
Unlimited Release
Printed May 2004

Innovative Design Approaches for Large Wind Turbine Blades
Final Report

TPI Composites, Inc.

Prepared by
Sandia National Laboratories
Albuquerque, New Mexico 87185 and Livermore, California 94550

Sandia is a multiprogram laboratory operated by Sandia Corporation,
a Lockheed Martin Company, for the United States Department of Energy's
National Nuclear Security Administration under Contract DE-AC04-94AL85000.

Issued by Sandia National Laboratories, operated for the United States Department of Energy by Sandia Corporation.

Available to DOE and DOE contractors from
U.S. Department of Energy
Office of Scientific and Technical Information
P.O. Box 62
Oak Ridge, TN 37831

Telephone: (865)576-8401
Facsimile: (865)576-5728
E-Mail: reports@adonis.osti.gov
Online ordering: http://www.osti.gov/bridge

Available to the public from
U.S. Department of Commerce
National Technical Information Service
5285 Port Royal Rd
Springfield, VA 22161

Telephone: (800)553-6847
Facsimile: (703)605-6900
E-Mail: orders@ntis.fedworld.gov
Online order: http://www.ntis.gov/help/ordermethods.asp?loc=7-4-0#online

SAND 2004-0074
Unlimited Release
Printed May 2004

INNOVATIVE DESIGN APPROACHES FOR LARGE WIND TURBINE BLADES FINAL REPORT

WindPACT Blade System Design Studies

TPI Composites, Inc.
373 Market Street
Warren, RI 02885

ABSTRACT

The goal of the Blade System Design Study (BSDS) was investigation and evaluation of design and manufacturing issues for wind turbine blades in the one to ten megawatt size range. A series of analysis tasks were completed in support of the design effort. We began with a parametric scaling study to assess blade structure using current technology. This was followed by an economic study of the cost to manufacture, transport and install large blades. Subsequently we identified several innovative design approaches that showed potential for overcoming fundamental physical and manufacturing constraints. The final stage of the project was used to develop several preliminary 50m blade designs.

The key design impacts identified in this study are: 1) blade cross-sections, 2) alternative materials, 3) IEC design class, and 4) root attachment. The results show that thick blade cross-sections can provide a large reduction in blade weight, while maintaining high aerodynamic performance. Increasing blade thickness for inboard sections is a key method for improving structural efficiency and reducing blade weight. Carbon/glass hybrid blades were found to provide good improvements in blade weight, stiffness, and deflection when used in the main structural elements of the blade. The addition of carbon resulted in modest cost increases and provided significant benefits, particularly with respect to deflection. The change in design loads between IEC classes is quite significant. Optimized blades should be designed for each IEC design class. A significant portion of blade weight is related to the root buildup and metal hardware for typical root attachment designs. The results show that increasing the number of blade fasteners has a positive effect on total weight, because it reduces the required root laminate thickness.

Acknowledgements

TPI Staff: Derek Berry and Steve Lockard
Dynamic Design: Kevin Jackson
MDZ Consulting: Mike Zuteck
University of California, Davis: Case Van Dam

Sandia Technical Monitors: Tom Ashwill
Paul Veers

TABLE OF CONTENTS

LIST OF FIGURES

LIST OF TABLES

1.0 ANALYSIS APPROACH

1.1 Goals and Objectives

The primary goal of the WindPACT Blade System Design Study (BSDS) was investigation and evaluation of design and manufacturing issues for wind turbine blades in the one to ten megawatt size range. The results of the initial engineering study [1] guided design specifications and preliminary engineering for candidate blades in the range of 30 to 70 meters in length. That initial project task was to assess the fundamental physical and manufacturing issues that govern and constrain large blades. The issues and constraints phase of the project entailed three basic elements: 1) a parametric scaling study to assess blade structure trends for current technology [1] , 2) a study of the cost to manufacture, transport, and install large blades [2], and 3) identification of promising innovative design approaches that show potential for moving beyond current physical and manufacturing constraints [3].

Subsequent work pursued the most promising avenues of advancement with preliminary blade designs for a 50m blade length. The first preliminary design approach used a fiberglass skin and fiberglass structural spar, while the second used a hybrid carbon/glass spar. Both designs sought to improve structural efficiency by tailoring the thickness of the blade cross-sections to simplify construction of the interior structural members. Inboard the blades used high thickness "flatback" inboard airfoils, while the outboard airfoil thickness was solved for the precise thickness and shape to yield the least complex and costly internal blade structure.

1.2 Summary of Parametric Study Results

The large blade parametric review [1] estimated peak power output, annual energy capture, design bending moments, blade laminate weight, and tip deflection for megawatt scale wind turbines with rotors of 62, 83, 104, 125, and 146 meters in diameter. The annual energy production for each rotor size was evaluated as a function of tip speed at 60, 65, and 70 m/s, which brackets the operating range of typical commercial wind turbines.

Blade design loads were estimated using two simplified methods: parked under extreme winds and an operating gust condition. The first model calculated the extreme loads with the turbine in the parked condition in accordance with IEC Class I design recommendations. The second calculation method estimated blade spanwise loading under high wind gust conditions. Both load estimation approaches provided similar results with regards to the blade design loads.

Structural analyses of three representative blades ("baseline", "thicker", and "thickest") were performed at representative spanwise stations. The blade construction was assumed to be a stressed shell, which was composed of four primary components: a low pressure shell on the downwind side, a high pressure shell on the upwind side, and two shear webs bonded between the two shells. The properties of the blade cross-sections were computed at several stations, which was used to estimate stress and deflection using standard two-dimensional beam theory.

In the range from 30 to 70 meters the blade weight grew as the cube of the length for all three representative blades studied. The economic performance of the blades is inversely related to the specific weight, which is defined as the blade weight divided by capture area (kg/m^2). Economics trends were negative over the range of blade diameter studied here; specific weight more than doubled over the analysis range.

Increased airfoil section thickness appears to be a key tool in limiting blade weight and cost growth with scale. Thickened and truncated trailing edges in the inboard region provide strong, positive effects on blade structural performance. For a given rotor radius, in moving from the thin to thickest blade distribution the specific weight was reduced by 15%, due to increased structural performance.

1.3 Summary of Cost Study Results

The cost study [2] reviewed critical fabrication and transportation constraints as a function of blade length. The cost of large wind turbine blades was estimated using an analytical model that was applied to each of the three blade sizes (30 m, 50 m and 70 m). The cost estimation approach assumed that currently available technology would be used and included materials, labor, development, facilities, and transportation costs. Laminate requirements obtained from the structural model were used to develop a bill of materials and manufacturing task list.

This study included important cost categories beyond materials and labor. Blade development costs included engineering design and documentation, fabrication of tooling and prototypes, and the cost of static, fatigue, and operational field testing. Facilities costs were calculated based upon the size of the rotor blades using manufacturing plant layouts developed specifically for each size. The costs of transportation were estimated assuming overland trucking from several different manufacturing locations. The study also identified potential constraints for movement of large blades on public roadways.

The results of the large blade cost study indicate that blade materials become a greater proportion of total blade cost, while the percentage of labor cost is decreased as blade size grows. Blade development costs were found to increase substantially with scale as a result of the higher prototype costs and the shorter production runs over which to amortize development costs. Transportation costs decreased as a percentage of total cost because total blade cost increased; however, size and weight limits were found to constrain shipment of blades larger than 50 meters and strongly influence transport costs of blades above that length.

The results of the large blade cost study indicate that overall blade cost scales at a rate less than the growth in the weight. This was due primarily to a lower rate of growth for manufacturing labor costs. Many of the labor cost categories were found to be proportional to blade length or area, rather than material volume. However, even with a more favorable scaling trend, the blade cost share as a percentage of the total turbine installed cost can be expected to nearly double as blade size increases from 30 to 70 meters. The large blade cost study also suggested that blade cost reduction efforts should focus on reducing material cost and lowering manufacturing labor requirements. Cost reductions in those areas were found to have the strongest impact on overall blade cost.

1.4 Innovative Design Study Results

The innovative design study [3] developed metrics to compare the structural and aerodynamic characteristics of different blade sections. This work indicated that inboard sections should be weighted more strongly toward structural performance, while outboard sections are weighted most highly on aerodynamic characteristics. The most direct method to increase blade section thickness is to scale existing airfoils. In addition to providing increased structural efficiency, this work showed that the use of specially designed inboard sections will minimize and potentially eliminate performance losses as compared to conventional airfoil sections. The innovative design study also documented a powerful method for designing the blade structure to minimize ply drops and simplify manufacturing. The concept of designing for simple structures before finalizing the aerodynamic design has not been widely applied in the wind energy industry heretofore, but the approach seems increasing appropriate as turbines grow larger.

The innovative design study investigated several material options that could be used to reduce blade weight. Carbon/glass hybrid provided excellent weight reduction, but presented some significant challenges for cost and manufacturing. The report recommended that further study of wood/carbon/glass hybrid (zebrawood) be supported. This material offers a number of benefits and appears to be cost effective.

Finally the innovative design study investigated the impact of IEC Design Class on the weight and cost of the blades. The results of the study show that the design class has a major impact on blade weight and cost.

1.5 Summary of Preliminary Design Results

The innovative approaches evaluation and preliminary design work assumed a reference blade length of 50 meters. The baseline blade planform characteristics are as shown in Table 1.1 and Figure 1.1 (Reynolds No. is at 10 m/s). The wind turbine was assumed to have a conventional, three bladed rotor with the blades mounted at the root to a central hub.

Table 1.1 Blade Planform Summary

Station Number	Radius Ratio	Twist (deg)	Chord (m)	Thickness (mm)	Thickness Ratio	Reynolds Number
1	5%	29.5	2.798	2798	100.00%	2.00E+06
2	15%	19.5	4.191	2640	63.00%	3.86E+06
3	25%	13.0	4.267	2341	54.87%	5.26E+06
4	35%	8.8	4.097	1756	42.86%	6.51E+06
5	45%	6.2	3.518	1204	34.23%	6.92E+06
6	55%	4.4	2.762	746	27.00%	6.51E+06
7	65%	3.1	2.218	532	24.00%	6.50E+06
8	75%	1.9	1.675	352	21.00%	5.28E+06
9	85%	0.8	1.232	234	19.00%	4.57E+06
10	95%	0.0	0.789	142	18.00%	3.12E+06

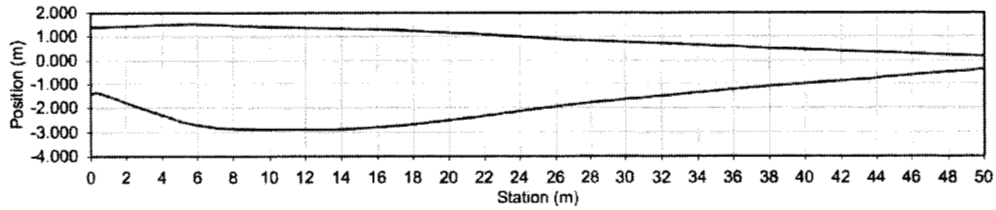

Figure 1.1 Blade Planform Graph

The preliminary blade design was developed assuming IEC Class III extreme wind design loads (Table 1.2). The analysis method assumed the wind speed was 52.5 m/s at the rotor hub and wind shear increased with hub height according to a power law. A wind shear exponent of 0.11, air density of 1.225 kg/m^3, and partial load factor of 1.35 were used as specified in the IEC standard. Blade aerodynamic forces were generated using the flat plate drag coefficient for the proper Reynolds number.

The preliminary design effort also assumed that the turbine operating parameters and control system response would maintain the peak operating loads at or below the extreme loads. This was a key assumption in the blade design and cannot be achieved without careful design of the turbine and its control system. It was assumed that operating gust loads could be held to similar levels by appropriate control strategies, with the possible use of advanced load control techniques such as bend-twist coupling. We believe that matching the operating loads to the extreme loads is a reasonable design approach that turbine designers will be able to meet. The edgewise loads were assumed to be proportional to gravity bending moment, with an appropriate multiplier to account for torque and fatigue.

Table 1.2 IEC Class III Blade Extreme Wind Design Bending Moments

Rotor Station (%)	Bending Moment (kNm)	Rotor Station (%)	Bending Moment (kNm)
0%	10407	50%	1652
10%	8010	60%	918
20%	5861	70%	439
30%	4085	80%	160
40%	2691	90%	32

The earlier innovative design study [3] identified substantial weight and cost advantages for truncated airfoils in the inner part of the rotor blade. For the preliminary design effort this concept was extended to the generation of a series of "flatback" airfoils whose thickness and trailing edge flat size could be specified separately. The flatback airfoils were not simply truncated versions of the reference airfoil; rather the selected trailing edge thickness was generated by hinging the upper and lower airfoil surfaces about the leading edge and adding that thickness at the trailing edge. This approach preserved the airfoil camber distribution, which would have been lost in the process of truncation. The flatback airfoil design method provided both additional shape flexibility, and more desirable section aerodynamics. In addition, higher lift outboard airfoil sections were used to reduce outboard planform area, thereby reducing bending moment to provide further weight and cost savings.

Through an iterative procedure, inboard blade thickness was adjusted to match flatwise moment requirements with a constant, buckling stable structural spar. Flatback width was adjusted to match edgewise requirements with a constant thickness trailing edge spline. Specifying blade thickness was an explicit variable provided the design freedom needed to eliminate ply drops from primary structure inboard of 55% radius station (r/R). A high lift and lift-to-drag (L/D) airfoil section was chosen for the tip (95%) airfoil to reduce bending moment through reduced outboard planform area, while an intermediate lift airfoil was specified at 75% r/R. Both the chord length and design Cl of these sections were "solved for" to allow the constant thickness spar cap to continue outward, with only a simple, material-efficient, linear width taper needed to match the flatwise moment requirements. The result is freedom from spar cap ply drops from root buildup until near the blade tip.

Two material choices were considered for the primary blade structure: E-glass and an E–glass/carbon hybrid, both with vinylester resin. Two root systems were considered, internal studs and T-bolts. Studs allow the possibility of saving root weight by using a higher count of smaller fasteners, so in addition to the case of sixty (60) 30mm fasteners, which is fairly typical of current large blades, other variations with one hundred twenty (120) 20mm fasteners were considered. Both meet minimum fastener strength calculations according to internationally recognized standards [4].

Previous design optimization work [1,2] focused on the weight and cost of the primary blade structure only (blade skins and spar caps). In the current work, this was extended to include the double-bias (DB) glass and balsa core used for the blade shell and shear webs, and other lesser components such as the trailing edge spline, gel coat, surface mat, shell and web bonding material. As core turned out to be a big cost component, buckling calculations were used to size the thickness of blade shell and web cores, rather than the rule of thumb estimates used previously. Additional weight contributions for resin in the core, and extra DB in the nose, were also added, to create more accurate weight and cost estimates appropriate for preliminary design.

It was found that the glass/carbon hybrid blade was about a ton lighter than the E-glass based blade, but the material cost was about $3,300 more. The materials cost of a 60 stud root was about the same as a 60 T-bolt root, but the stud root weighed almost a ton less. The 120 stud root was estimated to save nearly half a ton more weight, and about $1800, with further cost savings possible if a new, lower cost stud is proven to perform well.

2.0 PRELIMINARY DESIGN
OF STRUCTURALLY ENHANCED MULTI-MEGAWATT BLADES DESIGNED FOR EASE OF MANUFACTURING

2.1 Constant Thickness Primary Blade Structure

A primary thrust in creating a structurally optimized blade designed for ease of manufacturing was to design-in constant thickness for the primary blade structure in both the flatwise and edgewise directions, because constant thickness offers both structural and manufacturing benefits. In particular, elimination of laminate ply drops along the length will increase primary structure fatigue strength. The negative effect of ply drops has been documented in the literature [5] and has a large detrimental effect on the fatigue life curve. For this work we did not account for any benefits of fatigue strength improvement in the design allowables, so further weight and cost savings may be possible beyond those calculated here.

In addition to improved fatigue life, the long run of constant spar cap reduces the need to cut its materials, thereby reducing scrap and labor. Simplification of the spar cap lay-up would also be expected to save labor in the kitting and material placement operations. For the E-glass preliminary 50m design created in this study, the inboard blade spar cap was sized at 45.7mm (18") wide by 2.64mm (1.04") thick. This is the thickness of twenty (20) layers of a standard (C-520) unidirectional reinforcement, and could be cut from 91.4mm (36") or 137mm (54") wide rolls, or just ordered to width. In the outboard blade, a linear width taper is used, so that a single diagonal cut provides 100% usable material on both sides of the cut. These cost benefits to manufacturing were not credited in this phase of the work, but they are believed to be real and economically significant. Right from the start, the primary blade structure was designed for efficient manufacturing, with minimal labor and material costs.

2.2 The "AeroSolve" Design Process

The usual design process specifies the external blade shape first, and solves for the interior structure required to meet the loads within the given blade shape envelope. To achieve the advantages of constant thickness primary blade structure, this process must be inverted, with the structure specified first, and final aerodynamic shape solved for in subsequent steps. That this would be feasible, and result in an aerodynamically efficient blade, was not initially apparent. However, early work with thick, truncated inner blade airfoils gave spar caps without much variation along the span, once their thickness was adjusted to optimize weight and cost.

We performed a systematic investigation of the possible use of a series of inboard airfoils whose thickness and trailing edge flat could be independently adjusted to give constant thickness for both the spar caps that resist flatwise loads, and trailing edge spline that carries edge bending fatigue loads. This series of airfoil shapes was generated by combining a low pressure side shape drawn from the thick, high lift inboard NREL airfoils, and a structurally efficient high pressure side drawn from the LS–1 series airfoils. Representative shapes are shown in Figure 2.1. They have been named "flatback" airfoils, because the lift enhancing trailing edge flat doesn't truncate away part of the desired airfoil shape, thus giving improved aerodynamic performance, compared to the simple truncation employed in the earlier work.

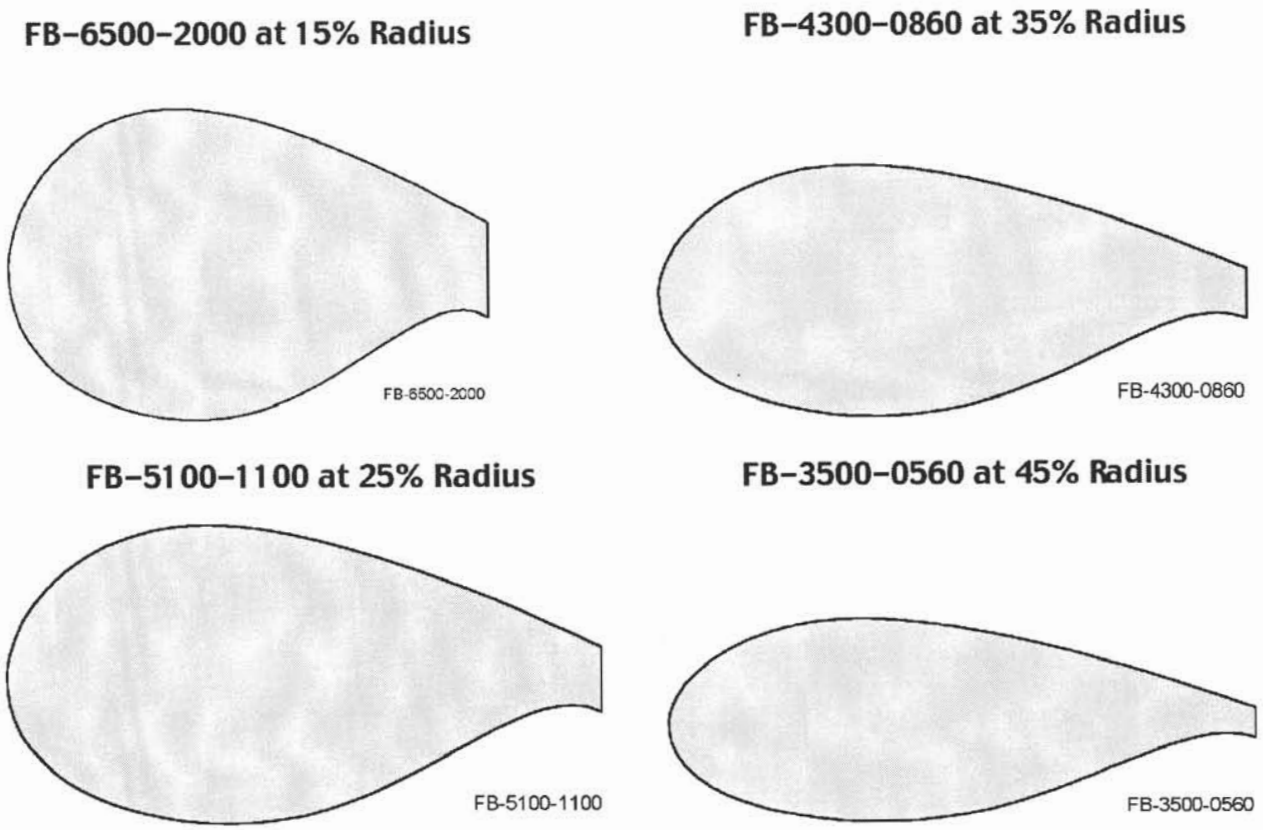

Figure 2.1 Representative Flatback Airfoils

An analysis of structural properties was performed at each inboard station. The section thickness was determined by iterating until the required flatwise moment capability was obtained for IEC Class III extreme wind loads. The flat trailing edge panel width was similarly adjusted so that an integral spline, composed of constant thickness reinforcing material, would provide the edgewise strength to meet the fatigue bending moment requirement.

For the outboard blade, the high lift NREL S831 airfoil was used to provide the required disk loading with reduced chord length, thereby reducing outboard blade planform area, and the blade flatwise bending moments associated with it (Figure 2.2).

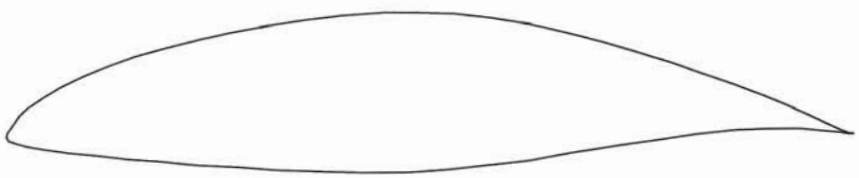

Figure 2.2 18% Thick S831 Airfoil for 95% Radius

For station 75% r/R, the airfoil was based on the thicker NREL S830 airfoil. Its chord length was adjusted to allow a linear spar cap width variation between stations 55% and 95% to meet the flatwise moment requirement, and a small adjustment was made to its camber line to tailor its Cl to the resulting chord length (Figure 2.3).

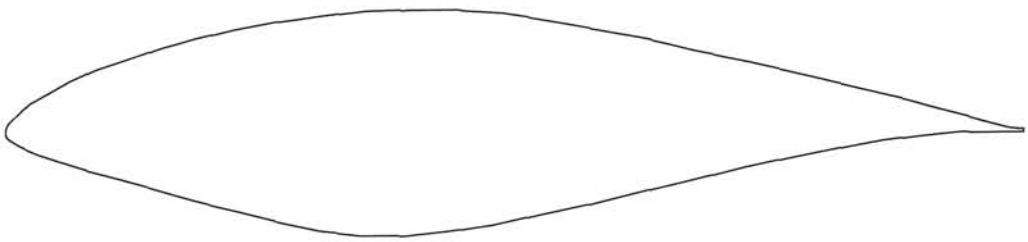

Figure 2.3 21% Thick S830 Airfoil for 75% Radius

For station 55% r/R, the 27% thick hybrid used for the earlier truncated inboard airfoil was again used, due to its favorable combination of structural efficiency and good aerodynamic performance (Figure 2.4).

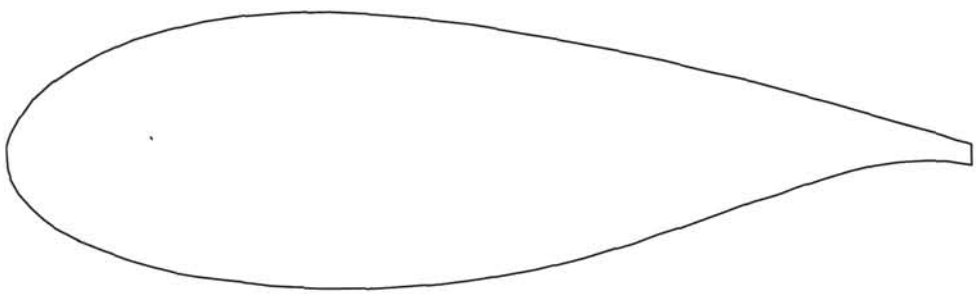

Figure 2.4 27% Thick Hybrid Airfoil for 55% Radius

2.3 Modifications from Previous Work

The most recent 50m blade preliminary design work was performed to a higher level of detail than the previous scaling and innovative design investigations [1,2]. This was done to provide more realistic weight and cost values, as befits a preliminary design. However, it also means that these values are no longer directly comparable with the earlier work, so the reader is cautioned against making such comparisons, which may be misleading.

Several changes were made in the way balsa core is handled. The earlier, simple estimates of core thickness based purely on panel free span were replaced with buckling calculations specific to each panel that accounted for both panel free span and curvature. Balsa was added between the forward edge of the spar caps and the nose, since this panel got wider with the use of a buckling-stable spar cap. A weight allowance for resin that fills the cuts that allow the balsa to contour into surface curvature was added.

Other changes included the addition of a layer of double bias fabric (DB1208) from nose to the aft edge of the spar cap, to provide additional leading edge strength, and further stabilize the spar cap, which was about twice as thick as in earlier work [2]. In recognition of shipping limits, the maximum blade chord was restrained to 4.27m (14'). Inboard of 15% of span, it was assumed that triangles of fiberglass reinforcement would be used to increase the spar cap width so it would become a complete circular tube of composite before reaching the root buildup. For the carbon hybrid blade, it was assumed that the carbon spar cap would end between station 15% and the root, once the widening fiberglass had lowered local strains to levels that made dropping out the carbon a less demanding design issue. This is done to avoid thermal expansion mismatch issues that might warp the blade root plane.

2.4 Blade Planform and Geometric Data

The preliminary design process started with a baseline planform, which was modified by solving for certain airfoil dimensions as described in the preceding discussion and resulted in the final preliminary design planform (Figure 2.5). It is characterized by a long region of nearly constant width near the maximum chord (sized by ground transportation constraints), and features a relatively narrow tip due to use of the high lift outboard airfoils. Beyond those features it looks quite normal, as it should, because it is designed to the same goals of efficient energy captures as the current generation of commercial large wind turbine blades. The differences between E-glass and carbon hybrid spar cap blades are too small to be seen at this scale.

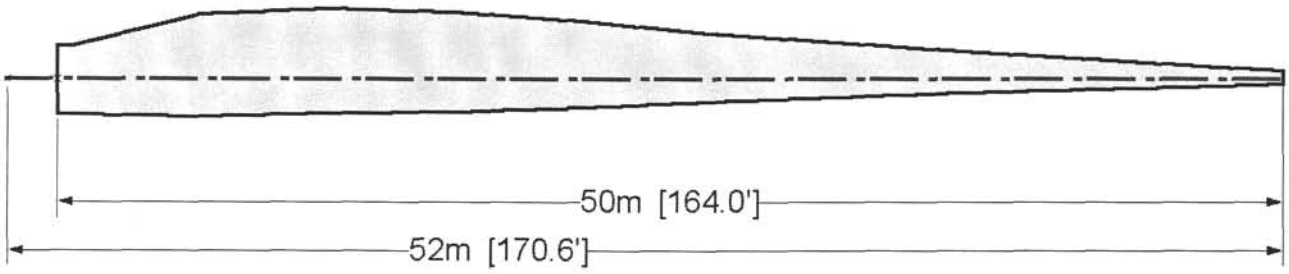

Figure 2.5 AeroSolve Preliminary Blade Planform

The primary geometric characteristics for the 50m aerosolve blades are provided in tabular form in Table 2.1. Note that the thickness ratio (t/c) and flatback trailing edge thickness differed slightly between the E-glass and carbon blades, so the values shown are the average of the two. The inboard airfoil nomenclature is FB for flatback, followed by section thicknesss and flatback thickness, both as percent of chord, with two digits behind the decimal place given. So the station 25% airfoil has a 54.87% t/c, with a flatback that is 12.16% of chord.

Table 2.1 Primary Geometric Data

Station Number	Radius Ratio	Twist (deg)	Chord (m)	Thickness (mm)	Thickness Ratio	Airfoil Type	Reynolds Number
1	5%	29.5	2.798	2798	100.00%	Circle	2.00E+06
2	15%	19.5	4.191	2640	63.00%	FB 6300-1800	3.86E+06
3	25%	13.0	4.267	2341	54.87%	FB 5487-1216	5.26E+06
4	35%	8.8	4.097	1756	42.86%	FB 4286-0802	6.51E+06
5	45%	6.2	3.518	1204	34.23%	FB 3423-0596	6.92E+06
6	55%	4.4	2.762	746	27.00%	FB 2700-0230	6.51E+06
7	65%	3.1	2.218	532	24.00%		6.50E+06
8	75%	1.9	1.675	352	21.00%	S830	5.28E+06
9	85%	0.8	1.232	234	19.00%		4.57E+06
10	95%	0.0	0.789	142	18.00%	S831	3.12E+06

Figure 2.6 shows the aerosolve blade chord and thickness distributions. The root region of the blade is essentially tubular, with smooth transition to a thickness-taper zone, which merges with a much thinner outboard blade region for aerodynamic efficiency where airfoil lift-to-drag ratio (L/D) is important.

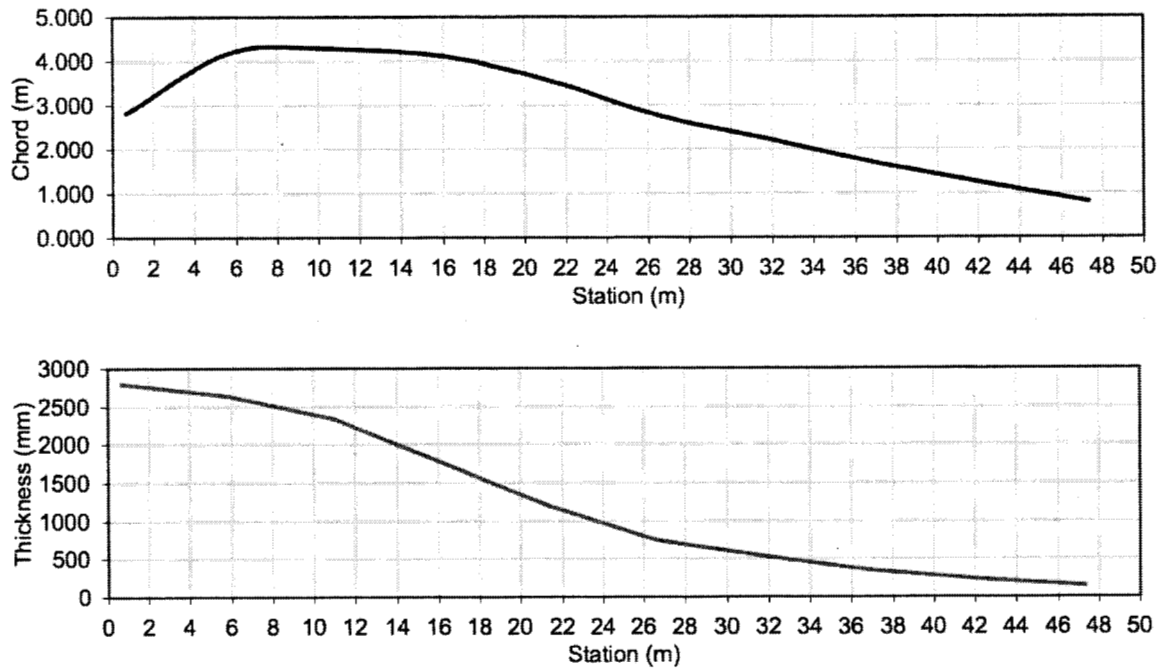

Figure 2.6 Planform & Thickness Distributions

Figure 2.7 illustrates the width taper of the spar cap and how it flares near the root to cover the entire root circle. The blade planform is also shown for perspective. It is evident that the flare at the root will drive down the local strains rapidly, since it is so much wider than the primary structural spar cap. Note that the vertical dimension has been expanded by about 2x to show the gentle linear taper in the outer blade, so the actual width taper in the root region is only about half that shown.

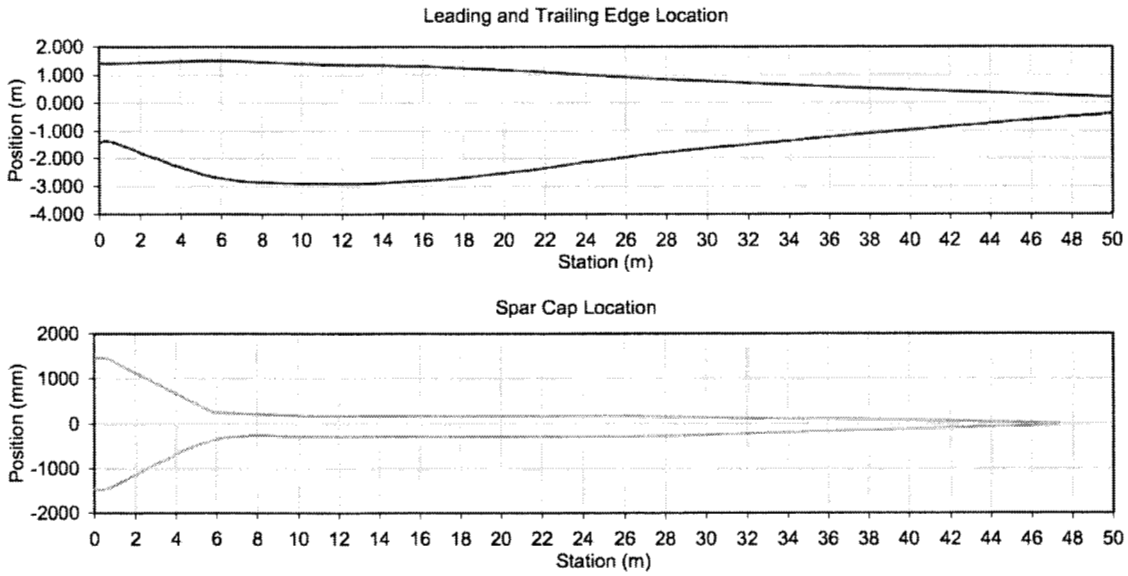

Figure 2.7 Spar Cap Width Taper Illustration for E-glass Design

Figure 2.8 shows the width of the E-glass and carbon hybrid spar caps in chart form. The E-glass spar cap is 457mm (18") wide by 26.4mm (1.04") thick in its constant width region, while the carbon hybrid is 356mm (14") wide by 21.3mm (.84") thick.

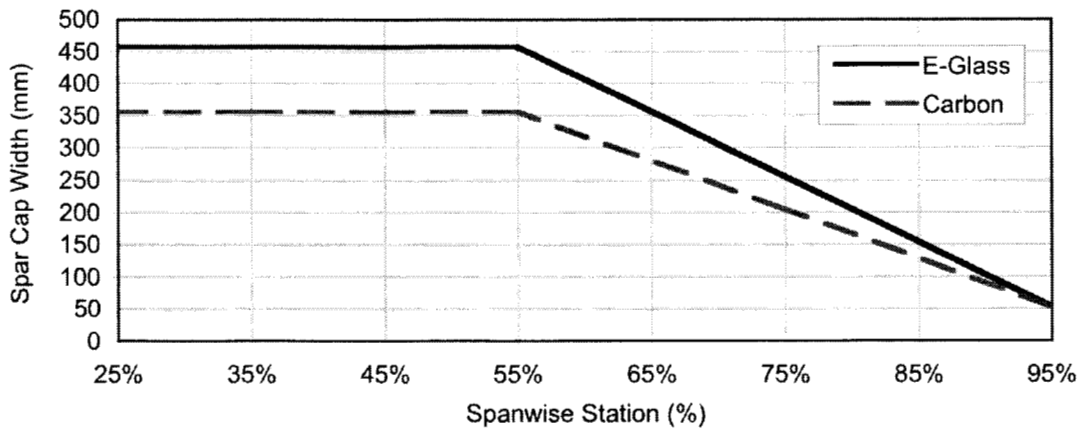

Figure 2.8 Outboard Spar Cap Width Taper

Blade Shell Weight and Cost Data

Tables 2.2 and 2.3 show the weight distributions and edgewise moment calculations for the E-glass and carbon hybrid blades, respectively. Note that the weight value shown is for the blade structure only; the root buildup and stud hardware weights have not been added at this point. The carbon hybrid blade shell is lighter by 879 kg, a 10% savings relative to the E-glass blade. Note that the carbon hybrid blade has E-glass DB (double bias) mixed into the spar cap material to improve its resistance to splitting, and that its aerodynamic shell is composed of the same E-glass DB and balsa core, just as the fully E–glass design. So it is not an extreme attempt to reduce weight by maximum use of carbon fiber. However, it does assume the carbon comes in at about 10% of span, and at current prices, many designers may still choose to stop it further outboard to save cost. Even with current prices, the cost difference for doing this will be shown to be moderate, and is likely to drop in the future, when this design practice may become common.

Table 2.2 E-glass Blade Weight and Edgewise Margin Distributions

Station % r/R	Section Weight (kg/m)	Chord (m)	Segment Weight (kg)	Segment CG % r/R	Weight to Tip (kg)	Gravity Edgewise Moment (kNm)	Spanwise T/E Force (kg) (2x gravity)	Shear Flow (kg/m) (2x gravity)	Blade Skin for Shear (mm)	Computed Edgewise Strength (kNm)	Edgewise Excess Margin
100%	8.3	0.53									
95%	21.1	0.76	38.7	97.1%	39	0.41	218			2.89E+01	1090%
75%	72.4	1.67	491.9	83.2%	531	23.9	5,836	562	0.015	1.59E+02	11%
55%	131.4	2.76	1072.0	64.0%	1603	123.2	18,250	1242	0.032	7.39E+02	0%
45%	175.8	3.38	808.1	49.8%	2411	220.4	26,625	1675	0.043	1.32E+03	0%
35%	233.2	3.94	1075.8	39.8%	3487	363.4	37,706	2217	0.057	2.19E+03	0%
25%	305.8	4.27	1417.8	29.8%	4904	567.1	54,316	3323	0.086	3.42E+03	0%
15%	345.6	4.03	1713.6	19.9%	6618	848.1	86,011	6341	0.164	5.07E+03	0%
5%	483.5	2.69	2181.2	9.7%	8799	1222.2	185,696	19943	0.515	1.78E+04	143%

Table 2.3 Carbon Blade Weight and Edgewise Margin Distributions

Station % r/R	Section Weight (kg/m)	Chord	Segment Weight (kg)	Segment CG % r/R	Weight to Tip (kg)	Gravity Edgewise Moment kNm	Spanwise T/E Force (kg) (2x gravity)	Shear Flow (kg/m) (2x gravity)	Blade Skin for Shear (mm)	Computed Edgewise Strength (kNm)	Edgewise Excess Margin
100%	10.2	0.53									
95%	20.2	0.76	40.1	97.2%	40	0.44	235			3.02E+01	1055%
75%	60.2	1.68	422.9	83.3%	463	21.62	5,264	503	0.013	1.56E+02	21%
55%	108.6	2.76	887.7	64.0%	1351	106.19	15,735	1047	0.027	6.36E+02	0%
45%	150.9	3.38	682.7	49.7%	2033	188.05	22,719	1397	0.036	1.13E+03	0%
35%	216.3	3.94	966.2	39.7%	3000	309.75	32,141	1885	0.049	1.87E+03	0%
25%	285.3	4.27	1319.7	29.8%	4319	487.29	46,674	2908	0.075	2.93E+03	0%
15%	299.9	4.03	1539.6	20.0%	5859	735.93	74,639	5595	0.144	4.42E+03	0%
5%	483.5	2.69	2061.0	9.6%	7920	1069.02	162,423	17562	0.453	1.78E+04	177%

The reader may note that the carbon blade shows a higher edgewise margin at the root than the glass blade, which is due to its lighter weight. The reason the margin is this large is that it was assumed for both designs that the full root tube is the 26.4mm (1.04") of glass laminate that matches the E-glass spar cap design. Except near the tip, the rest of the blade shows zero excess margin, because by design enough trailing edge spline was added to match the edgewise design requirement.

Tables 2.4 and 2.5 below give the weight and cost breakdown for the various materials of both the E-glass and carbon hybrid blades. The difference in cost for the carbon hybrid blade shell is $3,714. There is an extra column in the carbon glass hybrid table to show carbon spar cap costs. Note that a significant cost offset comes from reduced balsa core, even though the panel free spans are larger for the narrower carbon spar cap. This is because the lower design strain allowable for carbon allowed significantly thinner balsa core to satisfy the blade shell panel buckling requirements.

Table 2.4 E-glass Blade Material Weights and Costs

Station % r/R	Blade Weight (lbs/ft)	Material Weights by Type: Gel Coat (lbs/ft)	Mat (lbs/ft)	DB Glass (lbs/ft)	Spar Cap +TE (lbs/ft)	Balsa (lbs/ft)	Plexus/ Resin (lbs/ft)
100%	5.58	0.12	0.47	5.79	0.00	0.92	0.66
95%	14.17	0.17	0.67	8.67	1.23	2.44	0.99
75%	48.52	0.36	1.48	20.18	15.65	8.53	2.31
55%	88.11	0.62	2.53	35.72	29.96	15.32	3.96
45%	117.86	0.78	3.17	46.84	31.03	31.03	5.01
35%	156.34	0.94	3.81	58.76	32.81	54.03	6.00
25%	205.03	1.06	4.33	70.15	36.05	86.63	6.81
15%	231.72	1.04	4.23	72.42	67.10	80.17	6.76
5%	324.21	0.89	3.63	54.89	259.80	0.00	5.00
Weight (lbs)	19358						

	Gel Coat	Mat	DB Glass	Spar Cap +TE	Balsa	Plexus/ Resin
Weight of Material	106	433	6592	6468	5096	674
Percent of Blade Weight	1%	2%	34%	33%	26%	3%
Cost per Pound	$1.88	$1.05	$1.09	$1.10	$2.24	$4.00
Material Cost	$200	$453	$7,173	$7,138	$11,438	$2,695
Percent of Blade Shell Cost	1%	2%	25%	25%	39%	9%

Total Cost of Blade Shell Materials $29,096

Table 2.5 Carbon Hybrid Blade Material Weights and Costs

Station % r/R	Blade Weight (lbs/ft)	Material Weights by Type: Gel Coat (lbs/ft)	Mat (lbs/ft)	DB Glass (lbs/ft)	Spar Cap (lbs/ft) (carbon)	Root & TE (lbs/ft) (glass)	Balsa (lbs/ft)	Plexus/ Resin (lbs/ft)
100%	6.86	0.12	0.46	5.97	0.00	0.00	0.56	0.69
95%	13.56	0.17	0.67	8.83	0.94	0.00	1.94	1.02
75%	40.34	0.37	1.49	20.25	8.44	0.00	7.47	2.34
55%	72.79	0.62	2.53	35.72	15.70	1.06	13.17	3.99
45%	101.22	0.78	3.18	46.97	15.70	1.86	27.71	5.03
35%	145.05	0.94	3.84	59.31	15.70	3.13	56.08	6.06
25%	191.31	1.08	4.38	71.76	15.69	5.75	85.74	6.92
15%	201.11	1.04	4.23	72.23	15.72	35.97	65.16	6.76
5%	324.21	0.89	3.63	54.89	0.00	259.80	0.00	5.00
Weight (lbs)	17424							

	Gel Coat	Mat	DB Glass	Spar Cap	Root & TE	Balsa	Plexus/ Resin
Weight of Material	107	435	6634	1802	3076	4695	680
Percent of Blade Weight	1%	2%	38%	10%	18%	27%	4%
Cost per Pound	$1.88	$1.05	$1.09	$4.60	$1.10	$2.24	$4.00
Material Cost	$201	$455	$7,219	$8,285	$3,394	$10,538	$2,719
Percent of Blade Shell Cost	1%	1%	22%	25%	10%	32%	8%

Total Cost of Blade Shell Materials $32,810

2.5 Root Attachment Comparisons

Table 2.6 below shows the weight and cost for two primary root options, one based on bonded studs, and the other on T-bolts. For studs, it was found that the use of class III design loads allowed the use of 20mm fasteners, with studs that are only 190mm (7.5") long and 37mm (1.45") in diameter. Previous tests by TPI have shown that a stud this size can provide more than enough strength to match high grade 20mm bolts. To meet IEC bolted root design standards, it was found that 120 such studs would be required.

Table 2.6 Blade Root Attachment Weight and Cost Comparison

120 Stud Root			
Root Tube OD (ins)	105.91	Number of Studs	120
Root Tube ID (ins)	103.83	Weight of One Stud (lbs)	2
Buildup Thickness (ins)	1.5	Weight of Studs (lbs)	240
Length of Constant Thickness (ins)	8.0	Cost of One Stud	$30
Length of Taper (ins)	9	Cost of Studs	$3,600
Volume of Buildup (ins^3)	6077		
Density of Buildup Material	1.75		
Weight of Buildup (lbs)	384		
Cost per lb of Buildup Material ($/lb)	$1.10		
Cost of Buildup Material	$424	Total Root Materials Cost	$4,024

60 T-Bolt Root			
Root Tube OD (ins)	105.91	Number of T-Bolts	60
Root Tube ID (ins)	103.83	Weight of One T-Bolt (lbs)	9.17
Buildup Thickness (ins)	4.3	Weight of T-Bolt (lbs)	550.2
Length of Constant Thickness (ins)	18.9	Cost of One T-Bolt	$46
Length of Taper (ins)	25.8	Cost of T-Bolts	$2,760
Volume of Buildup (ins^3)	43805		
Density of Buildup Material	1.75		
Weight of Buildup (lbs)	2768		
Cost per lb of Buildup Material ($/lb)	$1.10		
Cost of Buildup Material	$3,055	Total Root Materials Cost	$5,815

The second option is a T-bolt root, with a more conventional fastener count of 60 30mm T–bolts. TPI has current cost experience with T-bolt hardware of this size, and with the dimensions of the root buildup needed to work with them.

The result of this cost comparison shows that a 120 stud count root may cost $1,791 less, and weigh 2694 lbs (1222kg) less, than a typical T-bolt root. The savings come entirely from the much smaller root buildup. The T-bolt hardware is less expensive than the studs, but the root buildup costs overcome this. Note that this is a materials comparison only, and capital equipment and labor costs have not been included.

As a check on what part of the savings was due to the higher stud count alone, estimates for a 60 stud root were also made. In that case, the weight advantage dropped to 1778 lbs (806 kg), but the cost was the same as the T–bolt root, within the accuracy of the data and assumptions. This raised the question of how well a high count T-bolt root might do, but there appears to be a packing limitation that may not allow such a T-bolt root without special measures to offset the close spacing. Due to lack of appropriate design experience, such a design was not pursued further at this time.

2.6 Blade Tip Deflection

Tables 2.7 and 2.8 provide a comparison of the predicted blade tip deflection under the design extreme wind loading. Most of the difference seen is due to the difference in the maximum compression strain allowable (fully factored) of 0.45% for fiberglass vs. 0.34% for the carbon hybrid blade, since the designs are otherwise very similar. The carbon hybrid blade also receives a small benefit from inner blade t/c values that are a little higher. This is a result of the narrower, thinner carbon spar cap having somewhat higher structural efficiency in the limited envelop at station 55% r/R.

Table 2.7 E-glass Blade Tip Deflection

E-Glass Station (r/R)	Station (ins)	Critical Distance (ins)	Tip Deflection Increment (ins)	Tip Deflection Increment (ins/%span)
5%	0	52.96		
15%	208	50.40	33.81	3.20
25%	415	45.04	32.35	3.08
35%	622	32.64	34.78	3.31
45%	830	22.53	41.98	3.99
55%	1037	14.68	51.87	4.93
75%	1451	6.88	125.35	5.96
95%	1865	2.94	117.89	5.60
100%	1969	1.47	10.93	2.08

	Strain	Tip Deflection (ins)	Tip Deflection (m)
E-Glass	0.0045	449	11.4

Table 2.8 Carbon Hybrid Blade Tip Deflection

Carbon-H Station (r/R)	Station (ins)	Critical Distance (ins)	Tip Deflection Increment (ins)	Tip Deflection Increment (ins/%span)
5%	0	52.96		
15%	208	50.24	25.59	2.42
25%	415	47.14	23.96	2.28
35%	622	33.81	25.22	2.40
45%	830	23.07	30.76	2.92
55%	1037	14.71	38.59	3.67
75%	1451	6.92	94.36	4.48
95%	1865	2.90	89.04	4.23
100%	1969	1.45	8.37	1.59

	Strain	Tip Deflection (ins)	Tip Deflection (m)
Carbon Hybrid	0.0034	328	8.3

2.7 Blade Frequencies

Tables 2.9 and 2.10 give the stiffness and weight data, and the resulting first natural frequencies for both the E-glass and carbon hybrid blades. Both blades have reasonable separation from 3p and 6p at rated rpm. The E-glass blade would allow considerable rpm reduction on a variable speed machine, while retaining good first frequency separation. The carbon blade first flatwise frequency approaches 6p with only a modest rpm reduction, but since flatwise motion is aerodynamically damped, this may be acceptable. The fact that flatwise and edgewise frequencies are much closer could begin to couple flatwise and edgewise modes, but it would only take a modest addition of material in the trailing edge spline to drive the frequencies further apart. Alternatively, the spline could be the same carbon hybrid material assumed for the spar cap, or carbon/wood/epoxy, both of which have much higher modulus to weight ratio, and are well suited to this use, with the higher mechanical damping of the wood perhaps providing a small added advantage for the latter choice.

Table 2.9 E-glass Blade First Frequencies and Stiffness

r/R	<--- Blade Station ---> (mm)	(ins)	Weight (lbs/ft)	Flatwise EI (lb-in^2)	Edgewise EI (lb-in^2)
5%	0	0	324.21	1.850E+12	1.850E+12
15%	5290	208	231.72	6.633E+11	1.153E+12
25%	10550	415	205.03	4.255E+11	7.282E+11
35%	15810	622	156.34	2.098E+11	4.505E+11
45%	21070	830	117.86	9.271E+10	2.416E+11
55%	26330	1037	88.11	3.568E+10	1.134E+11
75%	36850	1451	48.52	3.895E+09	1.440E+10
95%	47370	1865	14.17	8.991E+07	1.138E+09
100%	50000	1969	5.58	8.991E+06	1.138E+08
		Flatwise	**Edgewise**	**Flatwise**	**Edgewise**
First Frequencies		(Hz)	(Hz)	(p)	(p)
Non-Rotating		0.857	1.284	4.32	6.47
Rotating		0.893	1.306	4.50	6.58

Table 2.10 Carbon Hybrid Blade First Frequencies and Stiffness

r/R	<--- Blade Station ---> (mm)	(ins)	Weight (lbs/ft)	Flatwise EI (lb-in^2)	Edgewise EI (lb-in^2)
5%	0	0	324.21	1.850E+12	1.850E+12
15%	5290	208	201.11	8.739E+11	9.519E+11
25%	10550	415	191.31	5.875E+11	6.606E+11
35%	15810	622	145.05	2.870E+11	4.025E+11
45%	21070	830	101.22	1.257E+11	2.140E+11
55%	26330	1037	72.79	4.732E+10	1.007E+11
75%	36850	1451	40.34	5.189E+09	1.447E+10
95%	47370	1865	13.56	1.173E+08	1.179E+09
100%	50000	1969	6.86	1.173E+07	1.179E+08
		Flatwise	**Edgewise**	**Flatwise**	**Edgewise**
First Frequencies		(Hz)	(Hz)	(p)	(p)
Non-Rotating		1.054	1.304	5.31	6.57
Rotating		1.083	1.325	5.46	6.68

3.0 AERODYNAMIC PERFORMANCE OF STRUCTURALLY OPTIMIZED BLADE CROSS-SECTIONS

3.1 Background

The aerodynamic performance characteristics of the blade section shapes introduced in the previous chapter were analyzed using several different computational fluid dynamic (CFD) methods including the previously applied [1,3] viscous-inviscid interaction method MSES [6,7]. Because of concerns regarding the accuracy of this type of methodology for very thick airfoils and its validity for airfoils with significant trailing edge bluntness, the study progressed to several Reynolds-averaged Navier-Stokes (RANS) methods (INS2D [8,9], ARC2D [10], and OVERFLOW [11]). Standish & van Dam [12] present more information on these methods. Given the agreement between the solutions of the three RANS solvers as demonstrated in [12], the difficulties encountered applying INS2D to O-grids, and the fact that OVERFLOW requires about three times the computational resources of ARC2D because of its 3-D character, ARC2D was selected to provide RANS solutions fo the various section shapes.

ARC2D was developed by T. Pulliam and J. Steger at the NASA Ames Research Center [10]. The code solves the compressible, two-dimensional, Reynolds-averaged Navier-Stokes equations in strong conservation-law form. The governing equations in generalized curvilinear coordinates are central differenced in standard second-order form and solved using the implicit Beam-Warming approximate factorization scheme [13]. Artificial dissipation terms are added for numerical stability with the 2^{nd} order dissipation coefficient = 0.00 and the 4^{th} order dissipation coefficient = 0.64. Computations can be conducted in either steady-state or time-accurate modes. Steady-state calculations utilize space-varying timesteps for improved convergence rates, and the user is given the power to define mesh and timestep sequencing scenarios to further enhance computational efficiency. Time-accurate solutions can be run with a second-order accurate subiteration time-advancing scheme [14], in which the user can specify values for parameters such as the number of subiterations, physical timestep and pseudo timestep.

ARC2D contains an assortment of turbulence models with the one-equation Spalart-Allmaras model [15] used in the present study. ARC2D also has the option to use low-Mach number preconditioning that is meant to improve the solver accuracy and efficiency as the flow approaches incompressible conditions, but preconditioning was not utilized in this study. Due to the lack of any transition prediction models in the RANS solvers, all RANS free transition results in this study are, in fact, results obtained with transition specified at the locations predicted by using MSES. The transition prediction model incorporated in MSES is referred to as the "envelope method", which is a simplified version of the e^n method.

In this study, the primary grid generation tool for the RANS methods is a program called OVERGRID [16]. OVERGRID serves as a valuable tool for visualizing, constructing, manipulating, and diagnosing many types of grids and geometries. Two different grid types have been used in this study. C-grids (e.g., Fig. 3.1a and 3.1b) have been used for the various airfoils with sharp trailing edges while O-grids (e.g., Fig. 3.1c and 3.1d) were

used for all airfoils with a blunt trailing edge. As discussed in [17], the O-grid is arguably the most efficient gridding approach for any given airfoil geometry, but it has historically been shunned because of inadequate resolution of the airfoil wake.

Currently, researchers tend to select C-grids for nearly all 2D sharp trailing-edge airfoils because of its superior wake capturing characteristics and drag prediction capabilities. It too has drawbacks. The grid is inefficient in the sense that points are wasted in the wake-cut region of the grid where the normal spacing is very small near the airfoil surface due to requirements imposed by boundary layer thickness and turbulence models. The C-grid is also problematic when airfoils have finite thickness trailing edges.

While a C-grid is well suited for sharp trailing-edge sections, the modeling of non-sharp trailing edges is best accomplished with an O-grid in combination with properly chosen grid smoothing parameters. If smoothing parameters are improperly chosen or not used at all, the grid fans around the corners of the trailing edge creating two regions of sparse grid point distribution. The O-grid's historical shortcomings in terms of wake resolution can be overcome by clustering a large number of points in the trailing-edge region, particularly at the corners of the trailing edge. In the past, this was precluded by the computational expense of highly refined grids. However, with the advancement of computer technology, this restriction has vanished (at least in 2D) and an O-grid approach is a viable alternative to the use of a C-grid. Figure 3.1a shows a sample C-grid with a close-up of the trailing edge shown in Fig. 3.1b. Figure 3.1c and Fig. 3.1d show the O-grid for the identical airfoil. Comparison of the results on the O-grid and the C-grid were found to be in good agreement [12,17].

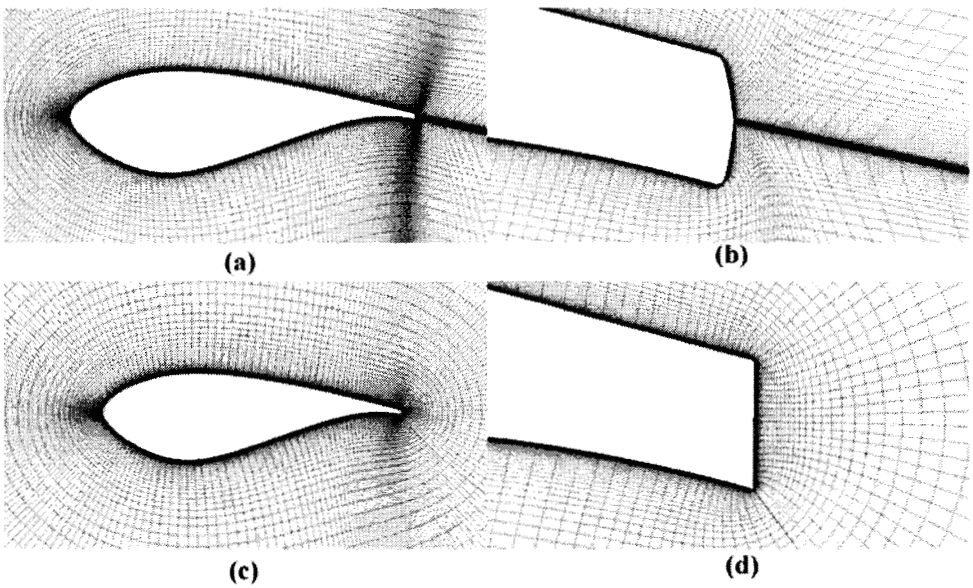

Figure 3.1 Close-ups of C-grid (a, b) and O-grid (c, d) used to compute flow about a 30% thick airfoil with 1.7% thick trailing edge [12].

All grids were constructed with the far field at a distance of fifty chord lengths. Various grid spacings were used on the surface of the airfoils but typically the spacings at the

leading and trailing edge corners ranged from 1×10^{-3} to 1×10^{-4} based on a unit chord. Stretching ratios in the range of 1.05-1.2 were used to define all surface points in between, typically resulting in 250-450 surface points. In the case of a C-grid, 75-100 grid points were placed on either side of the wake cut. The initial spacing in the direction of the outward normal was governed by the y^+ value of the turbulent boundary layer. Throughout this study, an outward normal spacing of 2×10^{-6} (based on a unit chord) was used at the surface and considered sufficient. A total of 125-150 grid points were used in the direction of the outward normal, with the first five points being equally spaced and the following being geometrically stretched. Grid refinement studies were conducted by doubling the grid density. The discrepancies between solutions were found to be negligible [12].

3.2 Inboard Flatback Airfoil Sections

As noted in Table 2.1, blunt trailing edge airfoils or so-called flatback airfoils were used to define the section shapes in the inboard region ($r/R \leq 55\%$) of the blade. The flatback airfoils provide several structural and aerodynamic performance advantages. Structurally, the flatback increases the sectional area and sectional moment of inertia for a given airfoil maximum thickness [3].

Aerodynamically, the flatback increases sectional maximum lift coefficient and lift curve slope and reduces the well-documented sensitivity of thick airfoils to surface soiling [12]. Figure 3.2 illustrates the beneficial effect of the flatback on the mean pressure distribution of an airfoil with a maximum thickness-to-chord ratio, t/c, of 35%. Sharp trailing edge airfoils with attached flows tend to have a trailing-edge pressure $C_p \approx 0.1$. However, suction surface flow velocities increase and the pressures along this surface decrease with increasing section thickness. For the airfoil shown in Fig. 3.2, the pressure coefficient reaches a low of $C_p = -2.7$ at $x/c = 0.1$. This combination of "fixed" exit pressure and decreasing upstream surface pressures with increasing section thickness leads to increased pressure recovery demands ($|\Delta C_p| = 2.8$ in Fig. 3.2). This in turn leads to premature onset of flow separation in the trailing edge region and consequently, a loss in lift.

The problem of premature trailing-edge flow separation is further enhanced by any loss of laminar flow due to blade surface soiling. Figure 3.2 presents pressure results for two 35% thick airfoils. The TR-35 airfoil has sharp trailing edge, while the TR-35-10 has a trailing edge thickness equal to 10% of the chord. The TR-35-10 decouples the suction and pressure sides of the airfoil allowing a decrease in the suction-side exit pressure. This in turn reduces the pressure recovery demands and mitigates trailing edge flow separation. From an airfoil performance point of view this results in increased maximum lift and reduced sensitivity to surface soiling. Of course, the blunt trailing edge does result in an increase in sectional drag and this is one reason why these airfoils are not recommended for use in the outboard blade region.

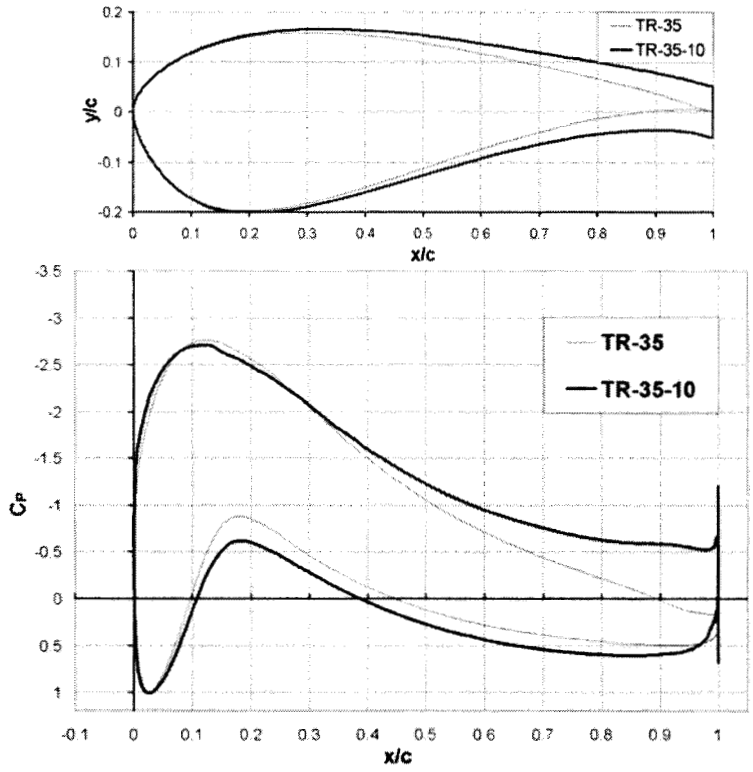

Figure 3.2 Effect of blunt trailing edge on mean pressure distribution at $\alpha = 8^{\circ}$, Re = 4.5 million, free transition [12].

The performance characteristics of the following flatback airfoils were analyzed at the Reynolds numbers indicated in Table 3.1. The section name FB xxxx-yyyy indicates a flatback airfoil with a maximum thickness-to-chord ratio, t/c, of xx.xx% and a trailing-edge-thickness-to-chord ratio, t_{te}/c, of yy.yy%. For instance, the most inboard section shape FB 6300-1800 has a t/c=63.0% and a t_{te}/c = 18.0%. These inboard sections are plotted and compared in Fig. 3.3. Their predicted performance characteristics are presented and compared in Fig. 3.4 through Fig. 3.10.

Both clean and soiled condition results are presented with the soiled conditions simulated by tripping the laminar boundary layer at x/c = 5% along both the upper and lower surface. Note, that these sectional results do not incorporate any 3D effects as a result of blade rotation. Also, the results do not include the effect of any 2D or 3D trailing-edge geometry modifications to alleviate the drag penalty associated with the blunt trailing edge. The effects of rotation and trailing-edge modifications will be discussed in some detail in Section 3.3. All results for the inboard sections were generated using the RANS method ARC2D.

Table 3.1 **Inboard section shapes and corresponding Reynolds numbers for normal operating conditions.**

Radial Station, r/R (%)	Section Name	Reynolds Number, Re
15	FB 6300-1800	3.86×10^6
25	FB 5487-1216	5.26×10^6
35	FB 4286-0802	6.51×10^6
45	FB 3423-0596	6.92×10^6
55	FB 2700-0230	6.51×10^6

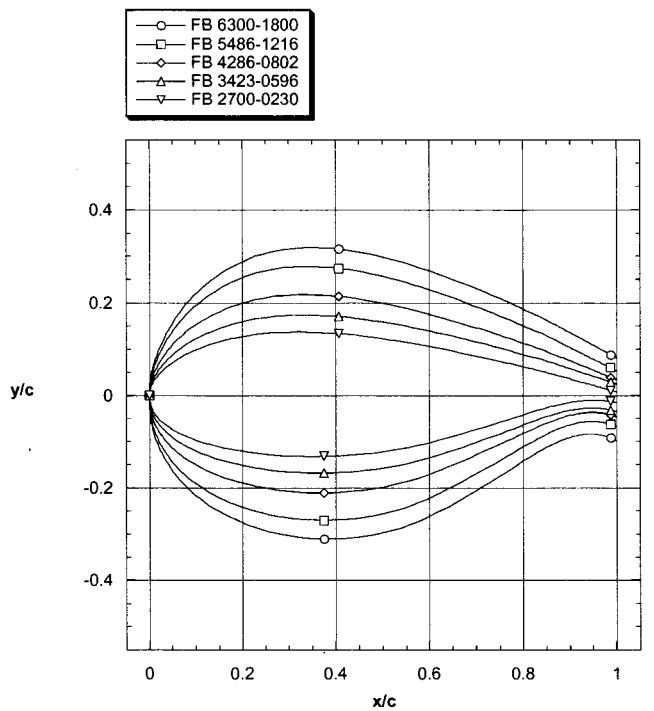

Figure 3.3 Inboard section shapes.

The results for the FB 6300-1800 are summarized in Fig. 3.4. At clean conditions, it is predicted to have a maximum lift coefficient of approximately 2.0 but its maximum lift-to-drag ratio remains below 20, mostly because of the large base drag penalty. At soiled conditions, the airfoil stops to perform as a lifting surface as marked by the lack of lift generation with increasing angle of attack.

Simulations for airfoils with the same t/c indicate that the sensitivity to surface soiling, even for this very thick airfoil, can be somewhat mitigated by increasing t_{te}/c. The flatback thicknesses selected here are a compromise driven by structural weight

considerations as explained in the previous chapter.

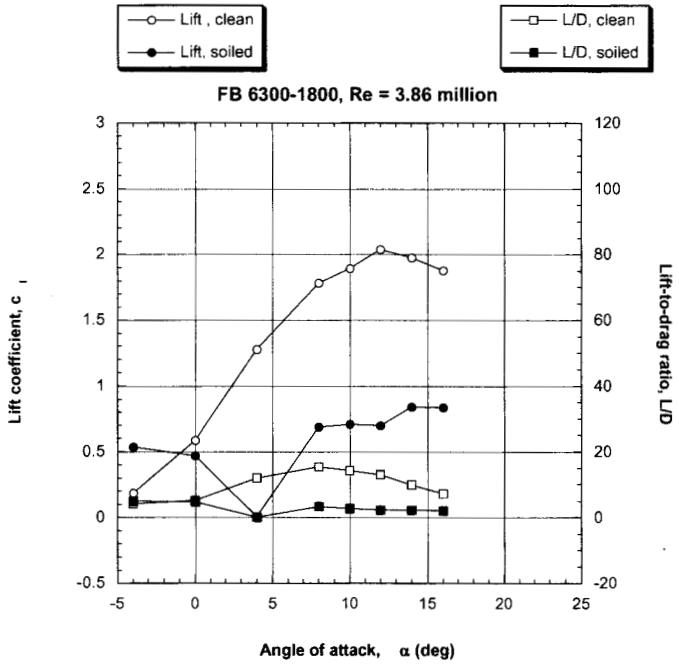

Figure 3.4 Lift and performance curves of FB 6300-1800. Soiled conditions modeled by tripping boundary layer at x/c = 0.05 on upper and lower surface.

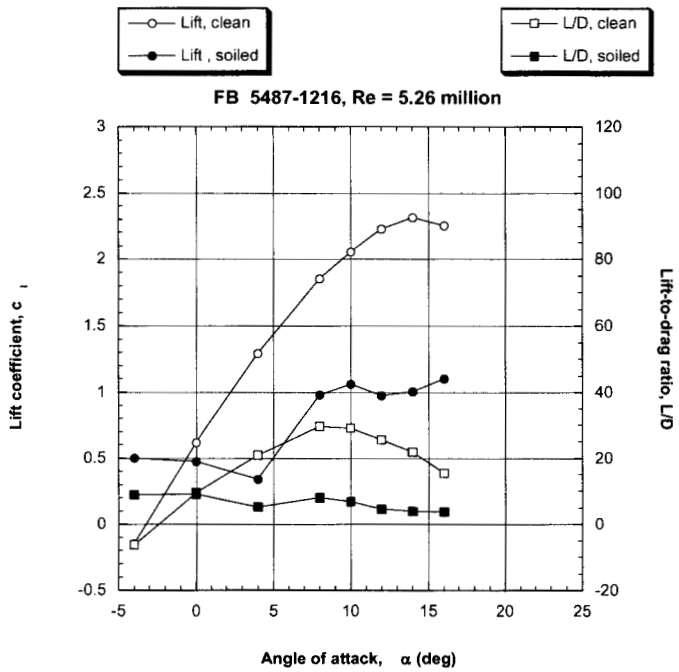

Figure 3.5 Lift and performance curves of FB 5487-1216. Soiled conditions modeled by tripping boundary layer at x/c = 0.05 on upper and lower surface.

The results for the FB 5487-1216 are summarized in Fig. 3.5. At clean conditions, it is predicted to have a maximum lift coefficient of approximately 2.3 and a maximum lift-to-drag ratio of approximately 30. At soiled conditions also this 55% thick airfoil demonstrates a lack of lift generation. Moving further outboard the sectional performance characteristics improve driven by the fact that the contribution to the overall wind turbine power performance becomes more critical with increasing radial station. The results for the FB 4286-0802, summarized in Fig. 3.6, demonstrate this improvement in performance. At clean conditions, this section shape it is predicted to have maximum lift coefficient of approximately 2.7 and a maximum lift-to-drag ratio of nearly 60. Also important is the fact that at soiled conditions the airfoil keeps on lifting as marked by the maximum lift coefficient of approximately 1.75.

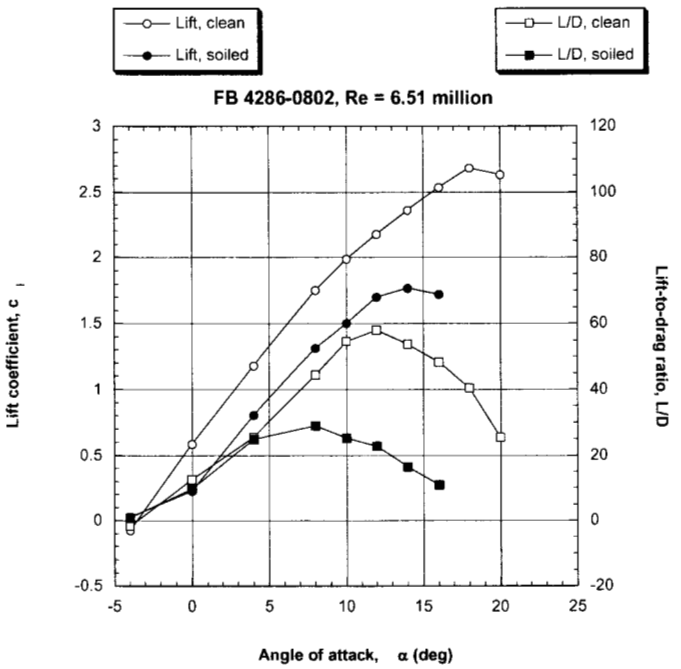

Figure 3.6 Lift and performance curves of FB 4286-0802. Soiled conditions modeled by tripping boundary layer at x/c = 0.05 on upper and lower surface.

The results for the FB 3423-0596 and the FB 2700-0230 are summarized in Fig. 3.7 and Fig. 3.8, respectively. At clean conditions, these section shapes are predicted to have maximum lift coefficients of approximately 2.5 and 2.0 and maximum lift-to-drag ratios of approximately 70 and 110. Soiled conditions cause a drop in the maximum lift coefficient of the FB 3423-0596 of 0.4 whereas the lift characteristics of the FB 2700-0230 are largely unaffected by soiling.

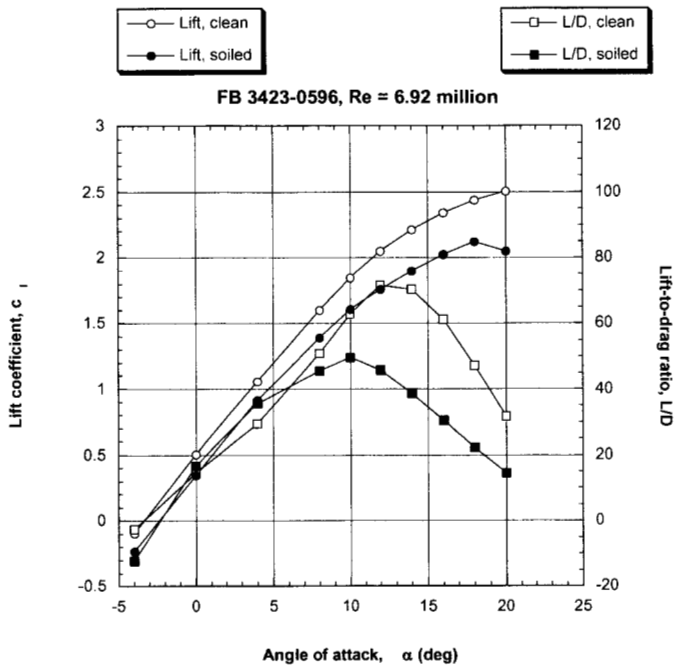

Figure 3.7 Lift and performance curves of FB 3423-0596. Soiled conditions modeled by tripping boundary layer at x/c = 0.05 on upper and lower surface.

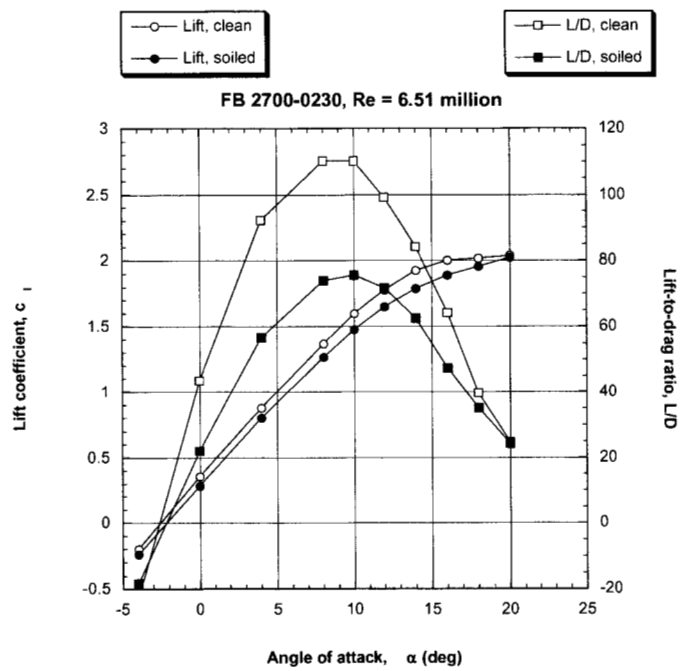

Figure 3.8 Lift and performance curves of FB 2700-0230. Soiled conditions modeled by tripping boundary layer at x/c = 0.05 on upper and lower surface.

The predicted lift results for the inboard flatback airfoils are compared in Fig. 3.9a and Fig. 3.9b at clean and soiled conditions, respectively. At clean conditions the 43% thick

FB 4286-0802 generates the highest maximum lift coefficient whereas at soiled conditions the thinner FB 3423-0596 and the FB 2700-0230 generate the highest lift values. The predicted lift-to-drag ratios for the inboard flatback airfoils are compared in Fig. 3.10a and Fig. 3.10b at clean and soiled conditions, respectively. At clean and soiled conditions, the 27% thick FB 2700-0230 generates the highest maximum L/D with this performance parameter dropping with increasing t/c and t_{te}/c for the other inboard airfoils.

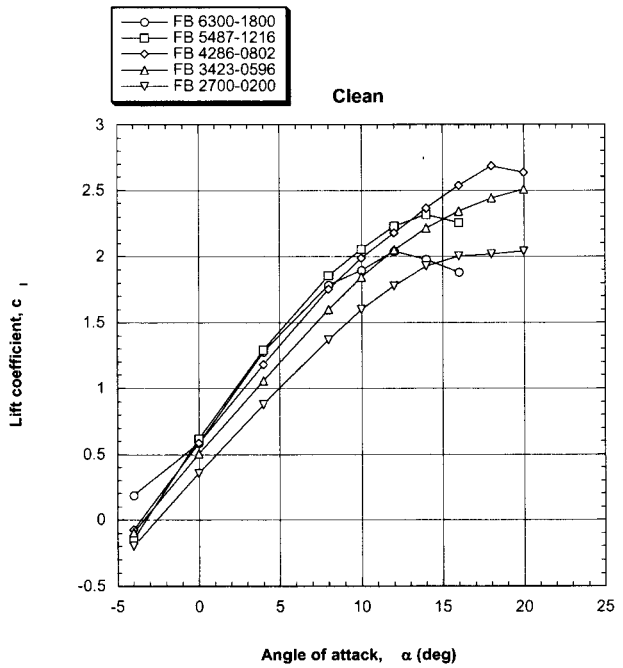

Figure 3.9a Comparison of section lift curves at clean conditions. Reynolds numbers as specified in Table 3.1.

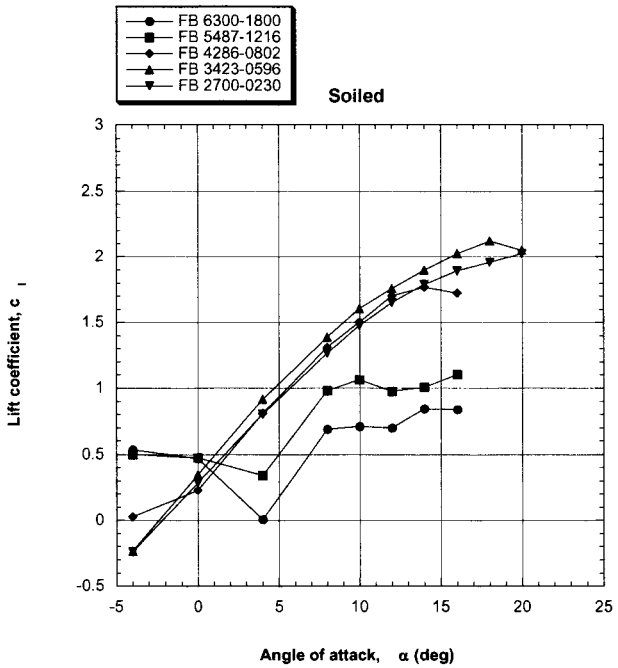

Figure 3.9b Comparison of section lift curves at soiled conditions. Reynolds numbers as specified in Table 3.1.

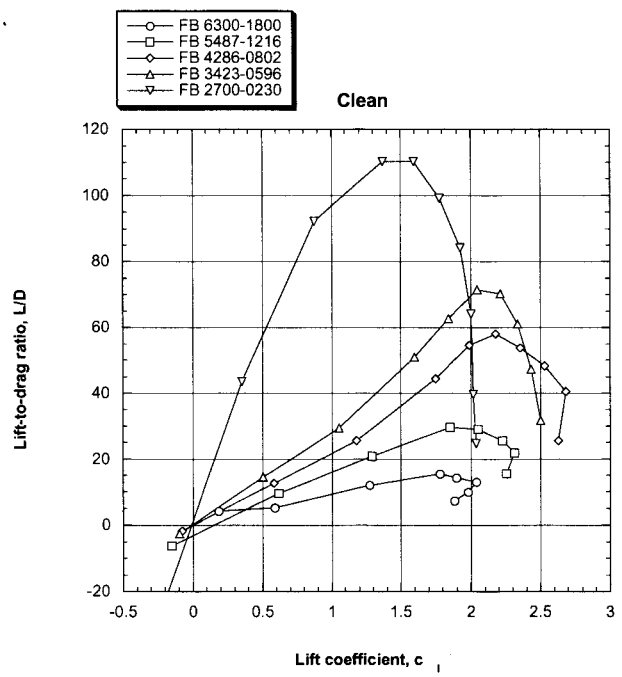

Figure 3.10a Comparison of section performance curves at clean conditions. Reynolds numbers as specified in Table 3.1.

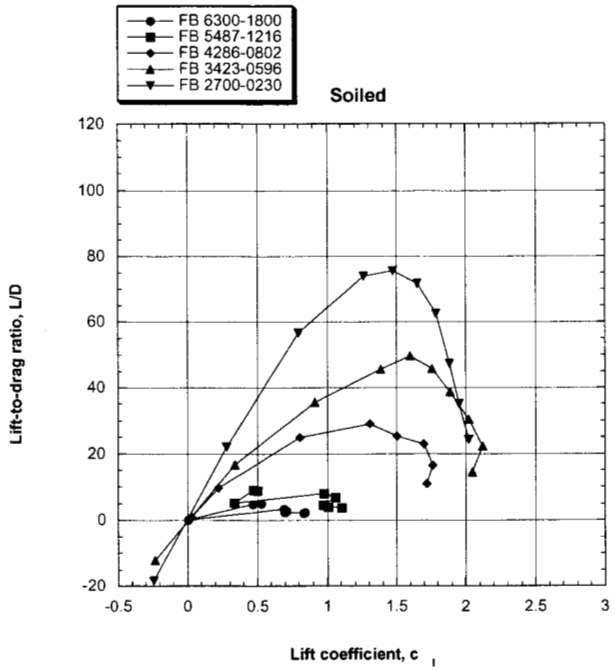

Figure 3.10b Comparison of section performance curves at soiled conditions. Reynolds numbers as specified in Table 3.1.

3.3 Outboard Airfoil Sections

More conventional, sharp trailing edge airfoils are selected for the outboard region. The performance characteristics of these airfoils were analyzed using MSES [12]. As mentioned previously, the performance predictions of MSES and ARC2D are compared and discussed in [12]. To provide some additional comparisons in the context of the present report, the performance characteristics of the FB 2700-0230 were computed using both methods. In Figure 3.11a and Figure 3.11b the performance predictions are compared at Re = 6.31 million and clean and soiled conditions, respectively.

For this airfoil with slightly blunt trailing edge (t_{te}/c = 2.3%), the lift results are in fair agreement with ARC2D predicting slightly higher maximum lift values. The lift-to-drag results show a larger discrepancy with MSES predicting slightly higher maximum L/D values. However, note that both maximum lift and maximum L/D are difficult to accurately calculate or measure in the wind tunnel [18,19]. Hence, the agreement between the two sets of predictions can considered to be fair and no performance prediction discrepancy is created by using ARC2D to calculate the 2D lift and drag values for the inboard blade region (where the more complex approach is necessary) and MSES for the outboard blade region (where the trailing edge is thin enough to apply MSES).

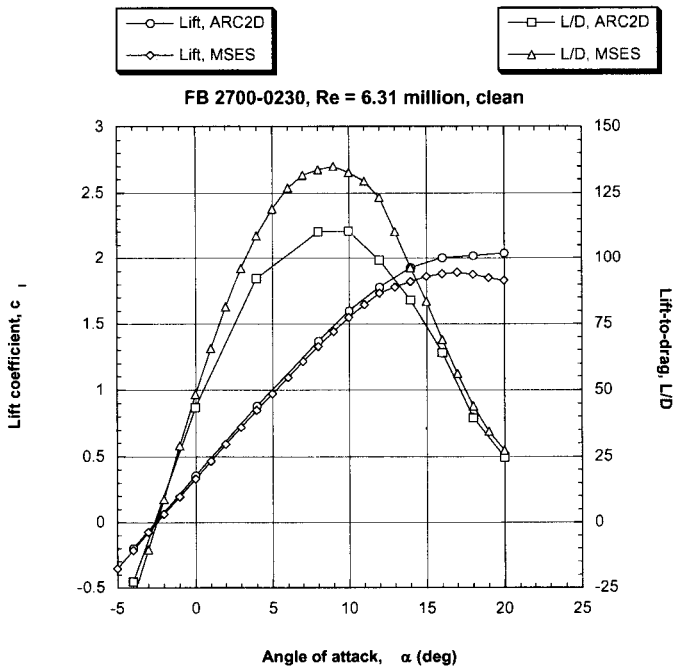

Figure 3.11a Comparison of FB 2700-0230 section performance characteristics at Re = 6.3 million and clean conditions.

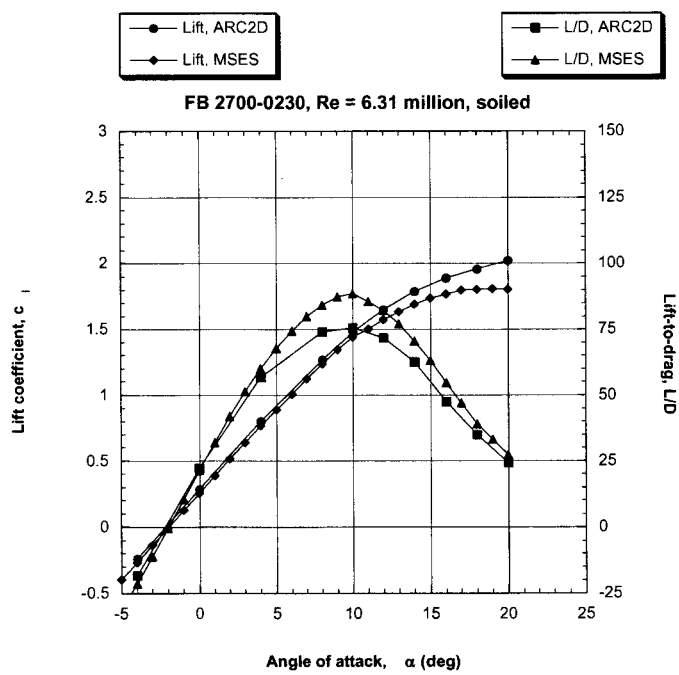

Figure 3.11b Comparison of FB 2700-0230 section performance characteristics at Re = 6.3 million and soiled conditions.

The NREL airfoil family for HAWTs was called upon to provide appropriate outboard section shapes. Initially the S817 and S816 were selected to define the section shapes in the tip (95% radius) and primary outboard region (75% radius), respectively. These airfoils were designed in 1992 for blades of stall-regulated wind turbines rated at 0.4-1.0 MW [20]. The fact that these airfoils were developed for stall-regulated rotors led to low design maximum lift coefficient of 1.1 for the S817 and 1.2 for the S816. However, the present rotor design is pitch regulated allowing for the application of section shapes that generate higher lift coefficients.

These higher design lift coefficients can be used to reduce sectional chord lengths (and, hence, lower rotor structural weight) and to achieve higher section lift-to-drag ratios (and, hence, increase rotor power coefficient). Tangler [21] suggested the S830 and S831 airfoils to provide outboard section shapes. The S831 is a tip airfoil (90% radius) with a maximum thickness-to-chord ratio of 18% and design maximum lift coefficient of 1.5. The S830 is a primary outboard tip airfoil (75% radius) with a maximum thickness-to-chord ratio of 21% and design maximum lift coefficient of 1.6. Table 3.2 lists the section shapes and corresponding Reynolds numbers, and Figure 3.12 depicts both section shapes.

Table 3.2 Outboard section shapes and corresponding Reynolds numbers.

Radial Station, r/R (%)	Section Name	Reynolds Number, Re
75	S830	5.28×10^6
95	S831	3.12×10^6

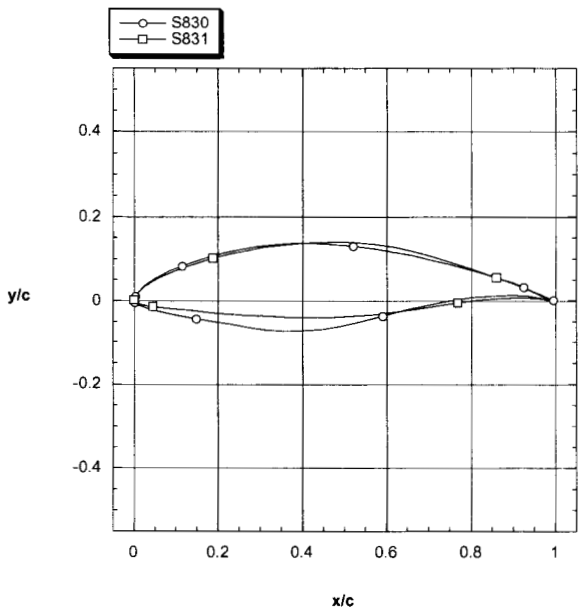

Figure 3.12 Outboard section shapes.

The MSES results for the S830 are compared against the S816 in Fig. 3.13 and summarized in Fig. 3.14. In Fig. 3.13a and 3.14, the S830 maximum lift prediction is

shown to match the design maximum lift coefficient of 1.6 which is unaffected by surface soiling. Also, the fact that the higher lift coefficient leads to higher lift-to-drag ratios at clean conditions as compared to the S816 is clear from Fig. 3.13b.

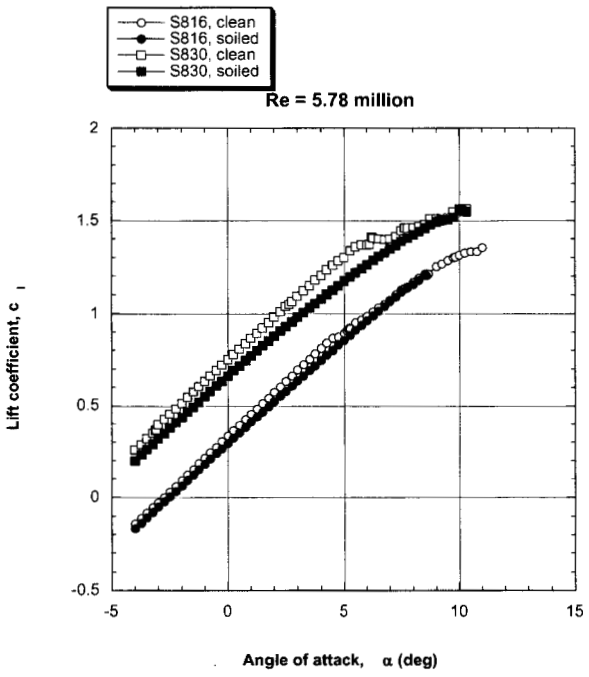

Figure 3.13a Comparison of S830 and S816 lift curves at Re = 5.78 million. Soiled conditions modeled by tripping boundary layer at x/c = 0.02 on upper and x/c = 0.05 on lower surface.

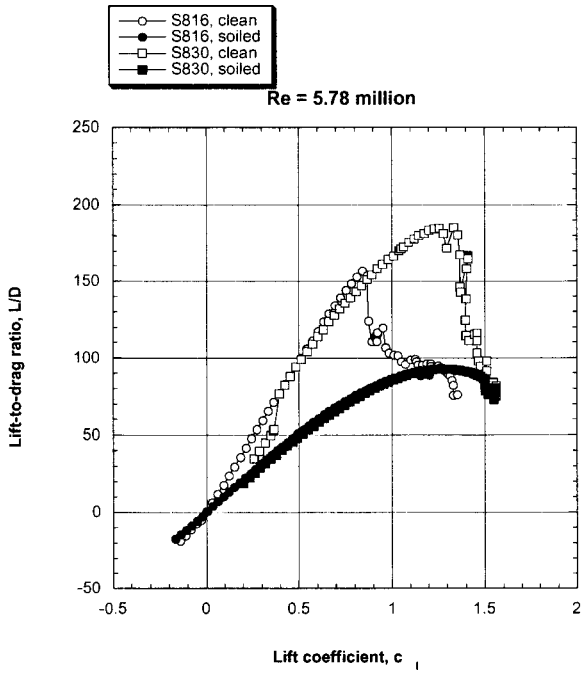

Figure 3.13b Comparison of S830 and S816 performance curves at Re = 5.78 million. Soiled conditions modeled by tripping boundary layer at x/c = 0.02 on upper and x/c = 0.05 on lower surface.

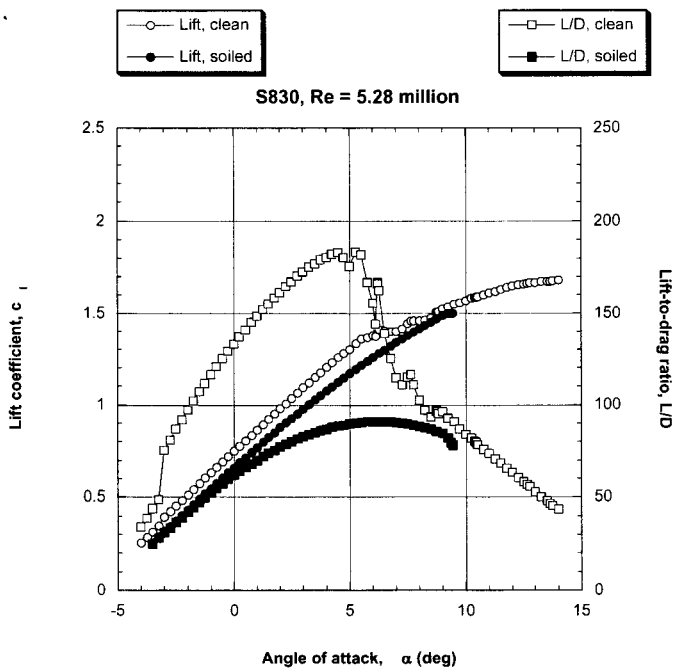

Figure 3.14 Lift and performance curves of S830 at Re = 5.28 million. Soiled conditions modeled by tripping boundary layer at x/c = 0.02 on upper and x/c = 0.05 on lower surface.

The results for the S831 are compared against the S817 in Fig. 3.15 and summarized in Fig. 3.16. Although the S831 achieves its design maximum coefficient of lift of 1.5, it does it at an angle of attack well above the angle of attack, α = 5-6°, at which the onset of flow separation occurs. This angle of attack is also the condition at which the lift-to-drag ratio reaches its maximum value. At soiled conditions, the lift curve leading up to stall is affected by the loss of laminar flow indicating that the high performance values this airfoil is capable of at clean conditions, as demonstrated by the $(L/D)_{max} > 200$, does appear to compromise somewhat its performance at soiled conditions.

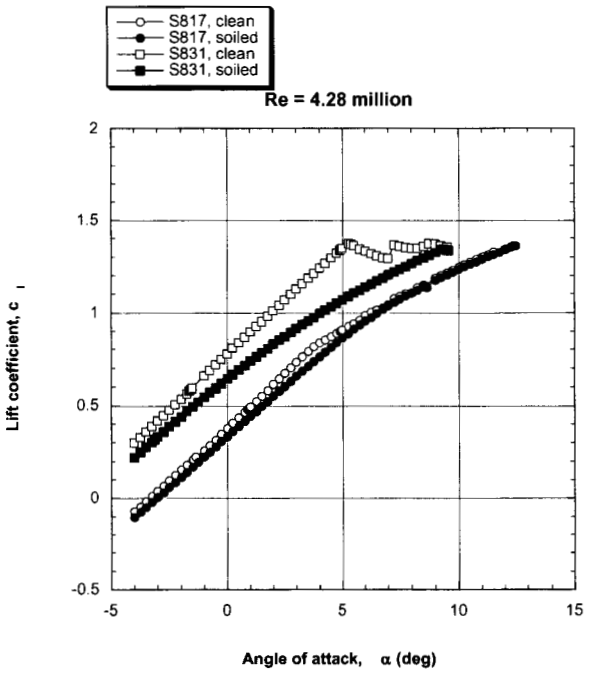

Figure 3.15a Comparison of S831 and S817 lift curves at Re = 4.28 million. Soiled conditions modeled by tripping boundary layer at x/c = 0.02 on upper and x/c = 0.05 on lower surface.

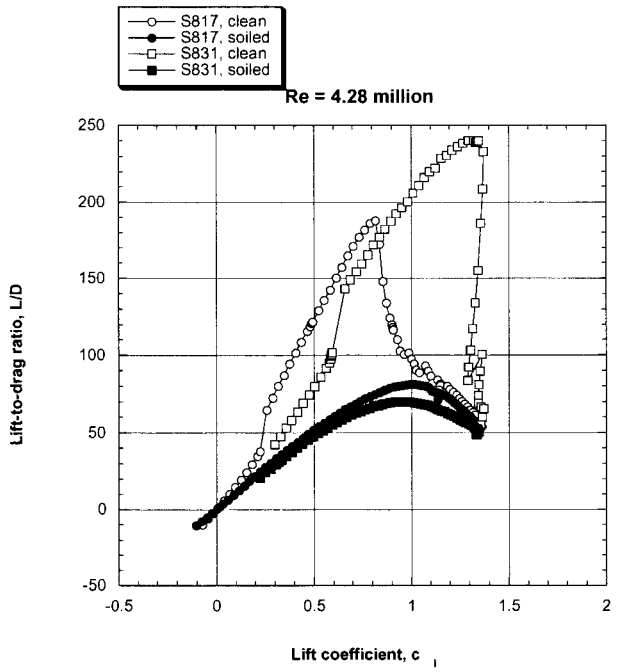

Figure 3.15b Comparison of S831 and S817 performance curves at Re = 4.28 million. Soiled conditions modeled by tripping boundary layer at x/c = 0.02 on upper and x/c = 0.05 on lower surface.

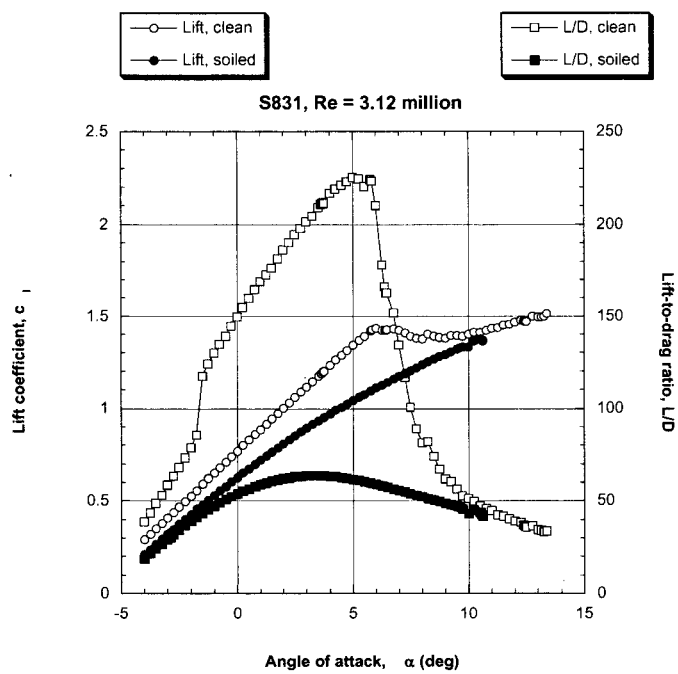

Figure 3.16 Lift and performance curves of S831 at Re = 3.12 million. Soiled conditions modeled by tripping boundary layer at x/c = 0.02 on upper and x/c = 0.05 on lower surface.

3.4 Discussion of Blade Section Performance

In this design study, significant attention has been paid to the inboard portion of the blade. The inboard region of large wind turbine blades contributes a relatively small portion of the overall torque generated by the entire blade due to the relatively small moment arm and low dynamic pressure when compared to the outboard region. However, improvements in aerodynamic performance will increase the overall efficiency of the wind turbine's power output. More importantly, the incorporation of blunt trailing edge airfoils in the inboard region will allow for thicker section shapes, providing increased structural stiffness while at the same time maintaining, if not increasing, aerodynamic performance. Thicker section shapes in the inboard blade region do not only provide the increased structural stiffness necessary for the larger wind turbines of the future, but could also help to mitigate the structural concerns, limitations, and cost of today's wind turbines.

Van Rooij and Timmer [22] point out that 3D rotational effects may lead to reduced roughness sensitivity for thick section shapes in the inboard region and this allows for the blade design in this region to be driven by structural demands. However, the extent of the roughness sensitivity mitigation due to rotational effects is fixed and governed by rotor size and rotational speed. In contrast, the incorporation of a blunt trailing edge into a blade design would give the designer even greater freedom to address structural demands while still maintaining control of the aerodynamic performance. Future efforts should focus on 3D RANS computations including blade rotation effects.

The main goal of wind turbine aerodynamics is to produce as much torque as possible in order to generate power while at the same time minimizing the thrust loads seen by the blades in order to reduce out-of-plane bending and structural concerns. Typically, the aerodynamic characteristics of a blade section are considered in terms of its lift and drag. However, when considering wind turbines, the importance of the lift and drag is secondary to that of the torque-force and thrust. For a given radial station, the lift and drag coefficients can be converted into torque-force, C_Q, and thrust, C_T, coefficients using the following relations:

$$\Phi = \alpha + \beta$$

$$C_Q = C_L \sin \Phi - C_D \cos \Phi$$

$$C_T = C_L \cos \Phi + C_D \sin \Phi$$

where α is the angle of attack and β is the twist angle relative to the plane of rotation. The sum of these two angles equates to Φ, the total angle of the relative wind to the rotor plane at a given radial station. The aforementioned angles and the force coefficients are depicted in Fig. 3.17. As can be gleaned from the above equation for the torque-force coefficient, the twist angle at a given radial station plays a significant role, particularly in the inboard region of the blade where twist angles are the greatest. Table 2.1 indicates that twist angles for the 15%-55% radial stations range from 19.5°-4.4°. In [12], the predicted lift and drag results for a 35% thick sharp trailing edge airfoil (TR-35) and an identical thickness flatback airfoil with a trailing-edge thickness of 10% (TR-35-10) were converted into torque-force and thrust coefficients to illustrate the secondary effect of drag on C_Q for a twist setting of 15°. The change in the torque-force coefficient,

$$\Delta C_Q = C_{Q_{TR\text{-}35\text{-}10}} - C_{Q_{TR\text{-}35}}$$

that results from the incorporation of a blunt trailing edge is plotted in Fig. 3.18. This plot shows that even without any trailing edge treatment to mitigate the base drag of the blunt trailing edge, a gain in C_Q is attained at the typical operating conditions of $\alpha \approx 8\text{-}15°$. This demonstrates that for the inboard blade region, the contribution to C_Q from the increased lift due to the flatback outweighs the penalty due to its increased drag thereby demonstrating that C_Q is mostly a function of lift and not drag [23].

The flow simulations indicate significant increases in drag, especially in the time-accurate solutions. The increase in drag for blunt trailing edges is primarily due to an increase in base drag caused by bluff-body vortex shedding and the resulting drop in pressure behind the trailing edge. There are a number of possible techniques that can be implemented to reduce the vortex shedding and consequently provide a significant decrease in base drag. The simplest example would be to add a splitter plate to the trailing edge that would project aft in the flow direction. A few test cases with splitter plates were evaluated and the results support the argument just presented. Other possible solutions include spanwise serrations along both the top and bottom surfaces and a flow cavity approach at the trailing edge. These concepts should be studied in the next phase of this study.

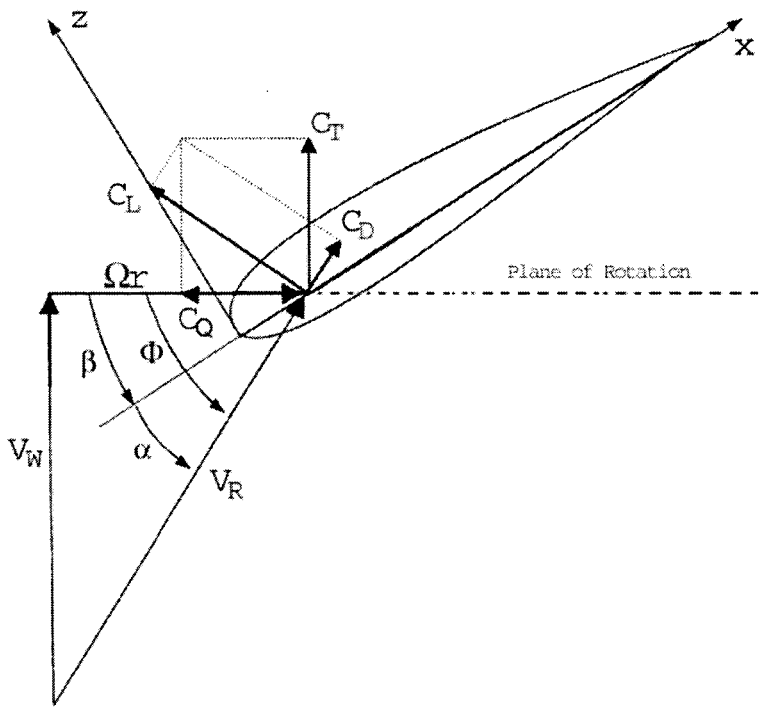

Fig. 3.17 **Relative orientation of C_Q and C_T to C_L and C_D with respect to the relative wind, V_R, and all pertinent angles at a given radial station [12].**

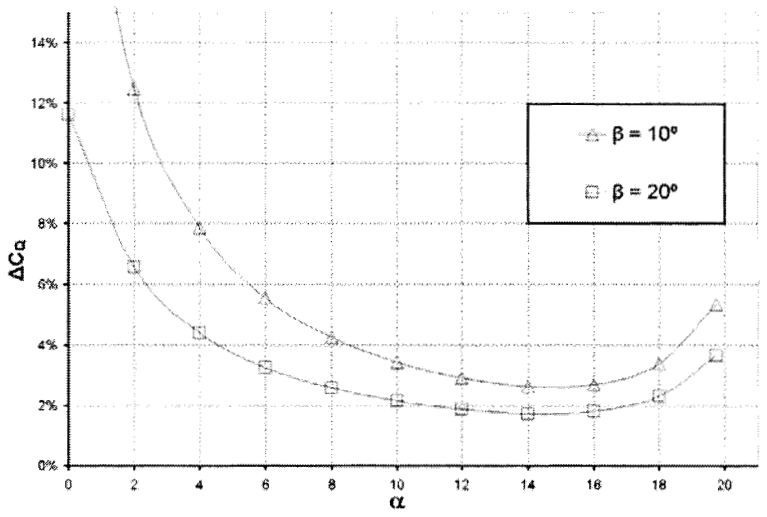

Fig. 3.18 Change in sectional torque-force coefficient, $\Delta C_Q = C_{Q_{TR-35-10}} - C_{Q_{TR-35}}$ due to blunt trailing edge [12].

3.5 Rotor Performance

Turbine power curves and annual energy estimates were developed using a performance model. The rotor aerodynamic performance was calculated using blade element momentum theory (PROP code). The turbine was assumed to have a rotor diameter of 104 meters, a rated power of 2.4 MW, active power regulation, and operate with variable speed. Standard air density was assumed (1.225 kg/m^3) and wind speed was assumed to be constant across the rotor disc. Gearbox performance losses were modeled assuming the gearbox losses were a constant 1.5 kW and the generator losses were assumed to be 60 kW at start-up, increasing to 240 kW at rated power.

Performance of the 50m preliminary rotor design was calculated assuming both clean and soiled blade conditions. The soiled rotor performance calculations used a linear model to evaluate the effects of blade surface soiling. The model assumed that soiling was proportional to the local section velocity and that inboard sections would have minimal soiling, while outboard the blade surfaces would be heavily soiled. The linear soiling model was used to calculate lift and drag properties for each spanwise blade section. The model assumed that the aerodynamic properties at 15% span were 85% clean (free transition) and 15% soiled (fixed transition). The lift and drag at mid span were an average of the free and fixed transition properties, while the properties at 95% span were 5% free transition and 95% fixed transition.

The preliminary rotor design provides excellent performance despite its extremely thick inboard section. With clean surfaces the rotor reached a peak power coefficient of 49%, which degraded slightly to 46% with soiled surface conditions (Figure 3.19). The clean and soiled power curves were also quite comparable (Figure 3.20, Table 3.3) and losses were primarily due to the increased skin friction associated with soiled blade surfaces.

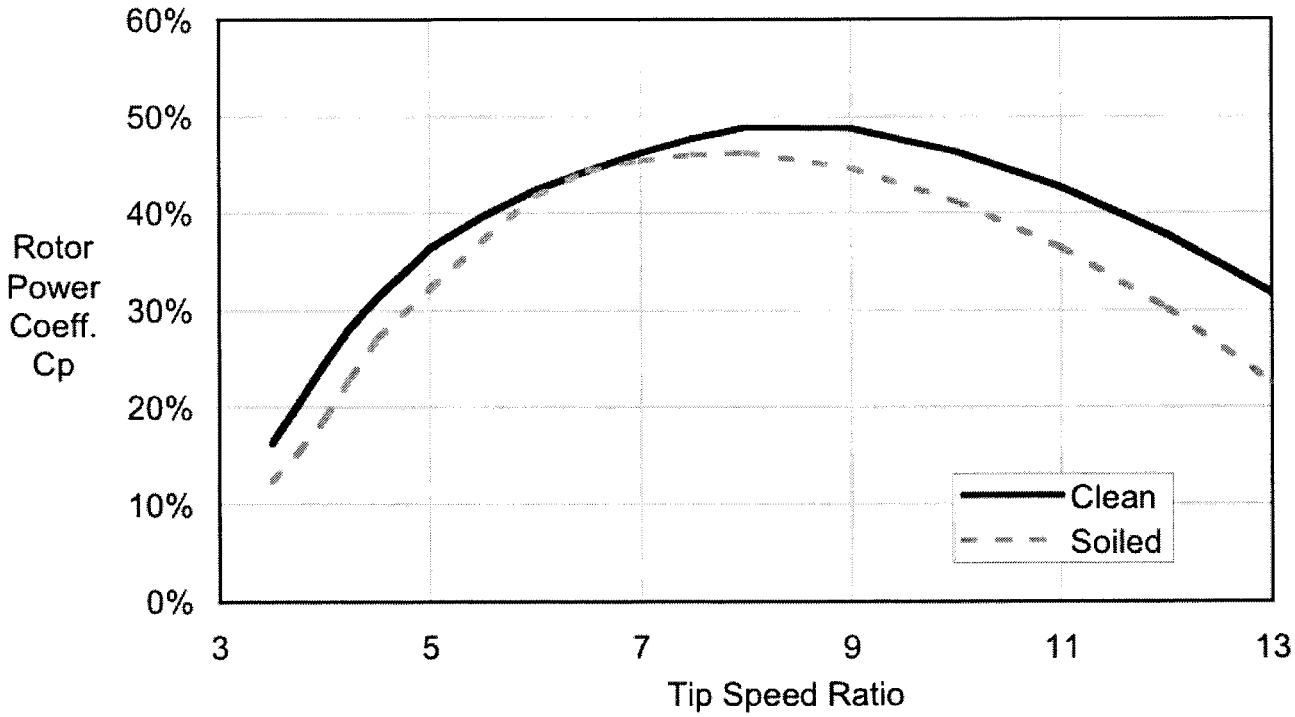

Figure 3.19 Rotor Power Coefficient for Clean and Soiled Surface Conditions

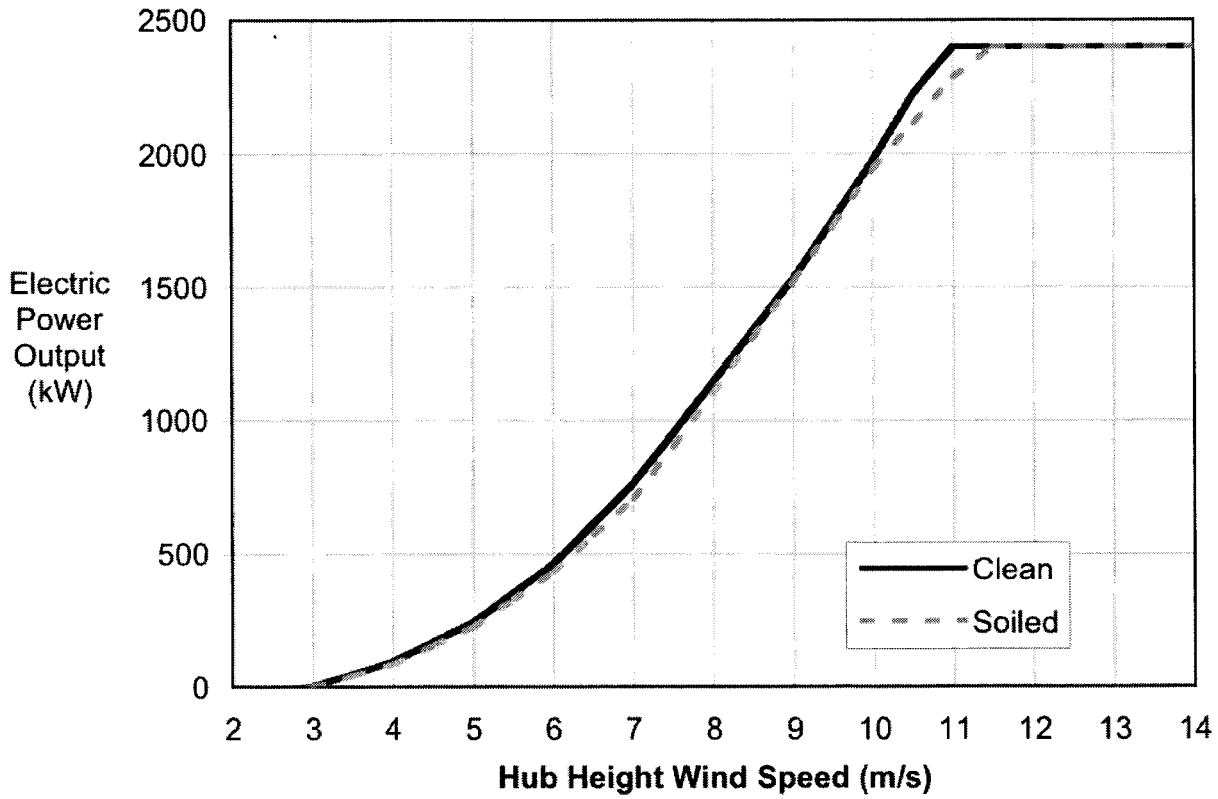

Figure 3.20 Power Curve Comparison for Clean and Soiled Surface Conditions

Table 3.3 Power Curve Comparison for Clean and Soiled Surface Conditions

Wind Speed (m/s)	Clean Surfaces (kW)	Soiled Surfaces (kW)	Power Difference (kW)	Power Difference (%)
4.0	93	85	8.3	9%
5.0	240	224	16.2	7%
6.0	460	432	28.1	6%
7.0	766	707	59.3	8%
8.0	1143	1102	40.8	4%
9.0	1532	1523	8.7	1%
10.0	1978	1949	29.1	1%
11.0	2400	2288	111.6	5%
12.0	2400	2400	0.0	0%
>12	2400	2400	0.0	0%

Annual energy capture was calculated for each of the four IEC specified wind classes, using the mean wind speeds associated with each class (Table 3.4). The energy capture calculations assumed a Rayleigh wind distribution and 100% turbine availability. The effects of blade soiling were relatively minor as a result of the roughness insensitivity of the airfoils used in the blade design. At the Class III site used for design of the blade the performance loss was slightly more that 2%.

Table 3.4 Annual Energy Capture at IEC Sites With Clean and Soiled Surface Conditions

IEC Wind Class	I	II	III	IV
Hub Height Mean Wind Speed (m/s)	10.0	8.5	7.5	6.0
Annual Energy With Clean Surfaces (MWh)	12678	10734	9053	6058
Annual Energy With Soiled Blade Surfaces (MWh)	12495	10531	8844	5862
Comparison Between Clean and Soiled Blades	1.4%	1.9%	2.3%	3.2%

4.0 CONCLUSIONS AND RECOMMENDATIONS

4.1 Summary of Key Design Impacts

4.1.1 Blade Cross-Sections

The results of this effort have shown that designing with thick blade cross-sections can provide a large reduction in blade weight, without compromising aerodynamic efficiency. Increasing blade thickness for inboard sections is a key method for improving structural efficiency and reducing blade weight. The flatback airfoils and the aerosolve design process were found to result in a blade design which had excellent power performance characteristics, especially with soiled surface conditions.

4.1.2 Alternative Materials

Carbon/glass hybrid blades were found to provide good improvements in blade weight, stiffness, and deflection when used in the main structural elements of the blade. The addition of carbon resulted in cost increases that were relatively modest, even at current pricing levels. Other material choices, such as S-glass and zebrawood (carbon/wood hybrid) are also worthy of additional study and offer potential benefits for weight and stiffness.

4.1.3 Blade Design Class

The changes between blades designed for a given IEC Design Class are significant and that may have implications of many sorts on how an "optimized" blade will be designed. Reductions in blade weight occur due to changes in design loads for the spar cap, trailing edge spline, and panel coring materials. The relative weight of a Class III blade was determined to be approximately 70% of a Class I design.

4.1.4 Root Attachment

This effort has shown that a great deal of the blade weight is tied up in the root buildup and metal hardware for typical root designs. A weight savings as large or larger than that available by shifting from E-glass to carbon hybrid spar caps may be available simply by moving to high count root stud systems, or high count T-bolts if their close spacing issues are reasonable to overcome. Its clear that a high part count would favor a single infusion operation for all the studs at once, so process innovation may be required before these gains can be attained efficiently and economically, but the weight savings does appear technically feasible.

4.2 Conclusions

The use of high thickness flatback airfoils in the inner blade, combined with the use of IEC Class III design loads, has lead to a large reduction in the amount of primary blade structure. This is dramatically illustrated by the fact that balsa coring is now the single largest material cost category. Blade costs have shifted toward being dominated by the aerodynamic shell to a somewhat remarkable extent, considering the size of the blades.

A comparison of blade set weight between the four preliminary blade designs (glass/stud, hybrid/stud, glass/T-bolt, and hybrid/T-bolt) and industry trends is provided in Figure 4.1. This graph uses data published by WindStats [24] in 2002 to show blade weight trends both for earlier designs and the latest wind turbine equipment. The present blade designs are significantly lighter in weight than the latest designs in the marketplace. This is partially the result of designing to IEC Class III design loads rather than Class II, but is also a result of improvements in the structural efficiency developed by the aerosolve design process employed in this work.

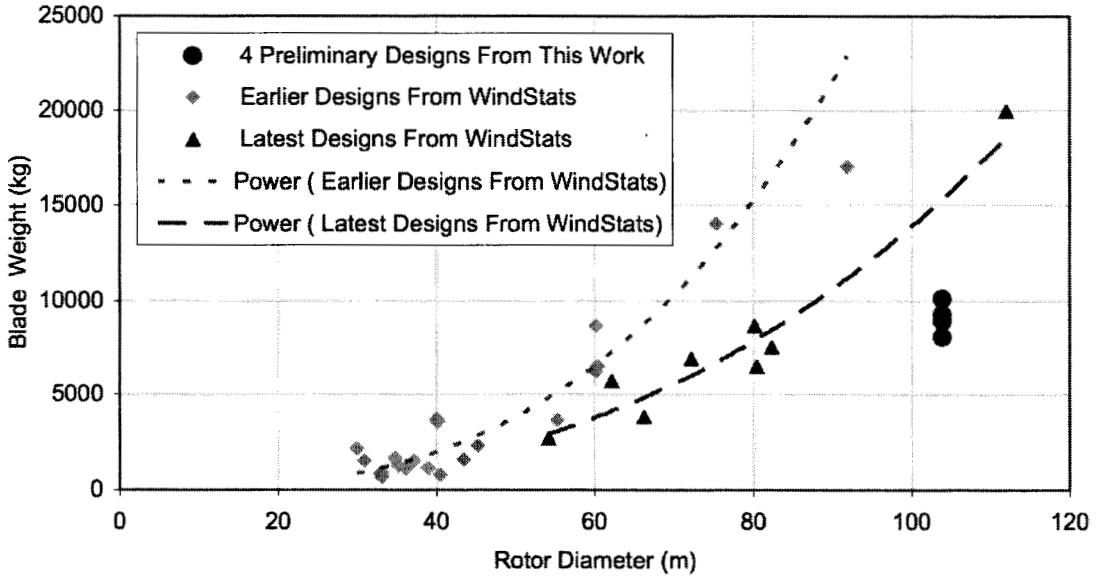

Figure 4.1 Comparison of Weight Trends to Between Preliminary Designs and WindStats Published Data

The ability of the aerosolve design process to yield constant thickness spar caps that run almost from root to tip extends the possibility of using preformed materials (pultrusions, dry preforms, etc.) as major spar cap constituents. Pultrusions may provide an efficient way to address fiber straightness, which has a strong effect on compression strength. They may also be a practical, cost effective way to achieve sweep/twist coupling [25]. Even if other material forms are not employed, this design process offers freedom from ply drops, and simplified cutting and placement, with very low material wastage. For a higher cost material such as carbon fiber, this could be a significant advantage no matter what form the carbon material takes.

5.0 REFERENCES

1 TPI Composites, "Parametric Study for Large Wind Turbine Blades", SAND2002-2519, August 2002.

2 TPI Composites, "Cost Study for Large Wind Turbine Blades", SAND2003-1428, May 2003.

3 TPI Composites, "Innovative Design Approaches for Large Wind Turbine Blades", SAND2003-0723, March 2003.

4 Systematic Calculation of High Duty Bolted Joints, Verein Deutscher Ingenieure, VDI 2230, Aug. 1988.

5 Mandell, J.F., et al., "Fatigue of Composite Materials and Substructures for Wind Turbine Blades", SAND2002-0771, 2002.

6 Drela, M., "Newton Solution of Coupled Viscous/Inviscid Multielement Airfoil Flows", AIAA Paper 90-1470, June 1990.

7 Drela, M., "Integral Boundary Layer Formulation for Blunt Trailing Edges," AIAA Paper 89-2166, 1989.

8 Rogers, S. E., and Kwak, D., "An Upwind Differencing Scheme for the Time Accurate Incompressible Navier-Stokes Equations", AIAA Journal, **28**(2), 1990, pp. 253-262.

9 Rogers, S. E., and Kwak, D., "An Upwind Differencing Scheme for the Steady-state Incompressible Navier-Stokes Equations", Journal of Applied Numerical Mathematics, **8**(1), 1991, pp. 43-64.

10 Pulliam, T.H., "Efficient Solution Methods for the Navier-Stokes Equations", Lecture Notes for the Von Karman Institute for Fluid Dynamics Lecture Series: *Numerical Techniques for Viscous Flow Computation in Turbomachinery Bladings*, Von Karman Institute, Rhode-St-Genése, Belgium, 1985.

11 Buning, P.G., Jespersen, D.C., Pulliam, T.H., Chan, W.M., Slotnick, J.P., Krist, S.E., and Renze, K.J., "Overflow User's Manual 1.8s", NASA Langley Research Center, Hampton, VA, 2000.

12 Standish, K.J., and van Dam, C.P., "Aerodynamic Analysis of Blunt Trailing Edge Airfoils", Journal of Solar Energy Engineering, Nov. 2003 (in press).

13 Beam, R., and Warming, R.F., "An Implicit Finite-Difference Algorithm for Hyperbolic Systems in Conservation Law Form", Journal of Computational Physics, **22**, 1976, pp. 87-110.

14 Pulliam, T.H., "Time Accuracy and the Use of Implicit Methods", AIAA Paper 93-3360, July 1993.

15 Spalart, P.R., and Allmaras, S.R., "A One-Equation Turbulence Model for Aerodynamic Flows", La Recherche Aérospatiale, (1), 1994, pp. 5-21.

16 Chan, W.M., "The Overgrid Interface for Computational Simulations on Overset Grids", AIAA Paper 2002-3188, 2002.

17 Mayda, E.A., "A CFD-Based Methodology to Automate the Generation of C-81 Airfoil Performance Tables", MS Thesis, Mechanical and Aeronautical Engineering, University of California, Davis, Aug. 2003.

18 Van Dam, C.P., "Recent Experience with Different Methods of Drag Prediction", Progress in Aerospace Sciences, Vol. 35, No. 8, 1999, pp. 751-798.

19 Van Dam, C.P., "On the Aerodynamic Design of Multi-Element High-Lift Systems", Progress in Aerospace Sciences, Vol. 38, No. 2, 2002, pp. 101-144.

20 Tangler, J.L., and Somers, D.M., "NREL Airfoil Families for HAWTs", NREL/TP-442-7109, Jan. 1995.

21 Tangler, J.W., Personal Communication, Feb. 2003.

22 Van Rooij, R.P.J.O.M, and Timmer, W.A., "Roughness Sensitivity Considerations for Thick Rotor Blade Airfoils", AIAA Paper 2003-0350, 2003.

23 Law, S.P. and Gregorek, G.M., "Wind Tunnel Evaluation of a Truncated NACA 64-621 Airfoil for Wind Turbine Applications", NASA CR-180803, 1987.

24 De Vries, E., "Multi-Megawatt Turbine Taking Hold", WindStats Newsletter, Vol. 15, No. 4, Autumn 2002.

25 Zuteck, M.D., "Adaptive Blade Concept Assessment: Curved Planform Induced Twist Investigation", SAND2002-2996, Oct. 2002.

DISTRIBUTION

J. Ahlgrimm
Office of Wind and Hydro Technology
EE-12
U.S. Department of Energy
1000 Independence Avenue SW
Washington, DC 20585

C. Arendt
HITCO Carbon Composites, Inc.
1600 West 135th St.
Gardena, CA 90249

H. Ashley
Dept. of Aeronautics and
Astronautics Mechanical Engr.
Stanford University
Stanford, CA 94305

K. Bennett
U.S. Department of Energy
GFO/Office of Project Management
1617 Cole Blvd.
Golden, CO 80401

K. Bergey
University of Oklahoma
Aero Engineering Department
Norman, OK 73069

D. Berry (5)
TPI Composites Inc.
373 Market Street
Warren, RI 02885

R. Blakemore
GE Wind
13681 Chantico Road
Tehachapi, CA 93561

C. P. Butterfield
NREL
1617 Cole Boulevard
Golden, CO 80401

G. Bywaters
Northern Power Systems
Box 999
Waitsfield,VT 05673

J. Cadogan
Office of Wind and Hydro Technology
EE-12
U.S. Department of Energy
1000 Independence Avenue SW
Washington, DC 20585

D. Cairns
Montana State University
Mechanical & Industrial Engineering Dept.
220 Roberts Hall
Bozeman, MT 59717

S. Calvert
Office of Wind and Hydro Technology
EE-12
U.S. Department of Energy
1000 Independence Avenue SW
Washington, DC 20585

J. Chapman
OEM Development Corp.
840 Summer St.
Boston, MA 02127-1533

Kip Cheney
PO Box 456
Middlebury, CT 06762

C. Christensen, Vice President
GE Wind
13681 Chantico Road
Tehachapi, CA 93561

R. N. Clark
USDA
Agricultural Research Service
P.O. Drawer 10
Bushland, TX 79012

C. Cohee
Foam Matrix, Inc.
1123 East Redondo Blvd.
Inglewood, CA 90302

J. Cohen
Princeton Economic Research, Inc.
1700 Rockville Pike
Suite 550
Rockville, MD 20852

C. Coleman
Northern Power Systems
Box 999
Waitsfield, VT 05673

K. J. Deering
The Wind Turbine Company
1261 120th Ave. NE
Bellevue, WA 98005

A. J. Eggers, Jr.
RANN, Inc.
744 San Antonio Road, Ste. 26
Palo Alto, CA 94303

S. Finn
GE Global Research
One Research Circle
Niskayuna, NY 12309

P. Finnegan
GE Global Research
One Research Circle
Niskayuna, NY 12309

P. R. Goldman
Director
Office of Wind and Hydro Technology
EE-12
U.S. Department of Energy
1000 Independence Avenue SW
Washington, DC 20585

R. Gopalakrishnan
GE Wind Energy
GTTC, 300 Garlington Road
Greenville, SC 29602

D. Griffin
GEC
5729 Lakeview Drive NE, Ste. 100
Kirkland, WA 98033

C. Hansen
Windward Engineering
4661 Holly Lane
Salt Lake City, UT 84117

T. Hermann
Wetzel Engineering, Inc.
P.O. Box 4153
Lawrence, KS 66046-1153

D. Hodges
Georgia Institute of Technology
270 Ferst Drive
Atlanta, GA 30332

W. Holley
GE Wind Energy
GTTC, 300 Garlington Road
Greenville, SC 29602

S. Hughes
NREL
1617 Cole Boulevard
Golden, CO 80401

K. Jackson
Dynamic Design
123 C Street
Davis, CA 95616

E. Jacobsen
GE Wind Energy
GTTC, 300 Garlington Road
Greenville, SC 29602

G. James
Structures & Dynamics Branch, Mail Code ES2
NASA Johnson Space Center
2101 NASA Rd 1
Houston, TX 77058

G. Kanaby
Knight & Carver Yacht Center
1313 Bay Marina Drive
National City, CA 91950

D. Kasperski
GE Wind Energy
GTTC, 300 Garlington Road
Greenville, SC 29602

M. Kramer
Foam Matrix, Inc.
PO Box 6394
Malibu CA 90264

A. Laxson
NREL
1617 Cole Boulevard
Golden, CO 80401

Bill Leighty
Alaska Applied Sciences, Inc.
P.O. Box 020993
Juneau, AK 99802

Wendy Lin
GE Global Research
One Research Circle
Niskayuna, NY 12309

S. Lockard
TPI Composites Inc.
373 Market Street
Warren, RI 02885

J. Locke, Associate Professor
Wichita State University
207 Wallace Hall, Box 44
Wichita, KS 67620-0044

D. Malcolm
GEC
5729 Lakeview Drive NE, Ste. 100
Kirkland, WA 98033

J. F. Mandell
Montana State University
302 Cableigh Hall
Bozeman, MT 59717

T. McCoy
GEC
5729 Lakeview Drive NE, Ste. 100
Kirkland, WA 98033

L. McKittrick
Montana State University
Mechanical & Industrial Engineering Dept.
220 Roberts Hall
Bozeman, MT 59717

P. Migliore
NREL
1617 Cole Boulevard
Golden, CO 80401

A. Mikhail
Clipper Windpower Technology, Inc.
7985 Armas Canyon Road
Goleta, CA 93117

W. Musial
NREL
1617 Cole Boulevard
Golden, CO 80401

NWTC Library (5)
NREL
1617 Cole Boulevard
Golden, CO 80401

B. Neal
USDA
Agricultural Research Service
P.O. Drawer 10
Bushland, TX 79012

T. Olsen
Tim Olsen Consulting
1428 S. Humboldt St.
Denver, CO 80210

R. Z. Poore
Global Energy Concepts, Inc.
5729 Lakeview Drive NE
Suite 100
Kirkland, WA 98033

J. Richmond
MDEC
3368 Mountain Trail Ave.
Newbury Park, CA 91320

Michael Robinson
NREL
1617 Cole Boulevard
Golden, CO 80401

D. Sanchez
U.S. Dept. of Energy
Albuquerque Operations Office
P.O. Box 5400
Albuquerque, NM 87185

R. Santos
NREL
1617 Cole Boulevard
Golden, CO 80401

S. Schreck
NREL
1617 Cole Boulevard
Golden, CO 80401

Brian Smith
NREL
1617 Cole Boulevard
Golden, CO 80401

J. Sommer
Molded Fiber Glass Companies/West
9400 Holly Road
Adelanto, CA 93201

K. Starcher
AEI
West Texas State University
P.O. Box 248
Canyon, TX 79016

A. Swift
University of Texas at El Paso
320 Kent Ave.
El Paso, TX 79922

J. Thompson
ATK Composite Structures
PO Box 160433
MS YC14
Clearfield, UT 84016-0433

R. W. Thresher
NREL
1617 Cole Boulevard
Golden, CO 80401

S. Tsai
Stanford University
Aeronautics & Astronautics
Durand Bldg. Room 381
Stanford, CA 94305-4035

W. A. Vachon
W. A. Vachon & Associates
P.O. Box 149
Manchester, MA 01944

C. P. van Dam
Dept of Mech and Aero Eng.
University of California, Davis
One Shields Avenue
Davis, CA 95616-5294

B. Vick
USDA, Agricultural Research Service
P.O. Drawer 10
Bushland, TX 79012

K. Wetzel
Wetzel Engineering, Inc.
PO Box 4153
4108 Spring Hill Drive
Lawrence, KS 66046-1153

R. E. Wilson
Mechanical Engineering Dept.
Oregon State University
Corvallis, OR 97331

M. Zuteck
MDZ Consulting
601 Clear Lake Road
Clear Lake Shores, TX 77565

M.S. 0557	T. J. Baca, 9125
M.S. 0557	T. G. Carne, 9124
M.S. 0708	P. S. Veers, 6214 (20)
M.S. 0708	T. D. Ashwill, 6214 (10)
M.S. 0708	S. Begay-Campbell, 6214
M.S. 0708	D. E. Berg, 6214
M.S. 0708	P. L. Jones 6214
M.S. 0708	D. L. Laird, 6214
M.S. 0708	D. W. Lobitz, 6214
M.S. 0708	M. A. Rumsey, 6214
M.S. 0708	H. J. Sutherland, 6214
M.S. 0708	J. Zayas, 6214
M.S. 0847	K. E. Metzinger, 9126
M.S. 0958	M. Donnelly, 14172
M.S. 1490	A. M. Lucero, 12660
M.S. 0899	Technical Library, 9616 (2)
M.S. 9018	Central Technical Files, 8945-1